

Answer

**Topic Editor Decision: Reconsider after major revisions** (05 Jan 2018) by John M. Huthnance  
Comments to the Author:

Dear Authors

Thank-you again for your revised version; you may now have seen the referee's comments on this revised version; for reference I have copied these comments below (sections A to I). The referee still wants to see your manuscript after further "major" revision (their term). Separately to me they have emphasised their concerns expressed in sections C, D, H below, and in respect of H also the question of the analysis for figure 8 also. I think the main message in all this is that your response to the referee's concerns should be embodied in your further-revised manuscript. The referee has emphasised that he does like the scientific significance of what you are writing about here, so please take all this as encouragement to clarify your manuscript as asked for.

Yours sincerely

John Huthnance

We thank the reviewer for the constructive comments and effort, which is helping much to improve the manuscript. We have taken all the comments and suggestions into account to rewrite a substantial part of the manuscript as indicated in our point-by-point answer below.

A) This manuscript presents a method of analysis aimed to quantify diapycnal diffusivity in the upper layers of the Alboran Sea using spectral methods. There are two major conclusions: first, it is possible to map the patchy nature of mixing in this data set. Second, there is a relationship between shear instabilities and mixing hotspots in the data but no correspondence between mixing and the location/amplitude of internal waves. The reported diffusivity levels generally match those found via using other methods: XCTD, ADCP, reference models.

As we mentioned above, we have modified the text in the new version of the m/s following the reviewer's comments. The first conclusion remains the same, but we have rewritten the part corresponding to the relationship between IWs, instabilities and mixing, which was confusing in the previous version. In summary, we do not mean that there is no relationship between IWs and mixing (we do not have direct evidence to discuss this and IWs are ubiquitous along the whole profile). What we say is that mixing appears to increase in areas with vigorous shear instabilities. Our interpretation is that shear instabilities are a mechanism enhancing energy transfer between IWs and turbulence (lines 19-22, 380-381, 441-447).

B) I think there is value in the results the authors attain. Products such as turbulence maps can teach us a lot about the oceanic interior and developing tools to do so using smaller seismic "high-res" hardware that can image the thermocline and shallow waters is a great step toward increasing the utility of seismic methods for oceanography. However, it is imperative to report findings as clearly and robustly as possible. I recognize that spectral methods are not the new innovation of this manuscript and am familiar with Sheen et al. 2009; Holbrook et al., 2013; and

Sallares et al., 2016; and the sliding analysis window for tracked seismic reflections is not a fundamentally new methodology either, as in Fortin et al., 2016. That said, I do consider this a new method due to the application to higher resolution data; it is not obvious that findings with large systems as in Sheen (2009) and Holbrook (2013) will equally apply to smaller systems. Additionally, using only tracked reflectors and a sliding window analysis has not been done, to my knowledge. Further, Sallares et al., 2016 is a short-format paper that shows only 1 spectra of the average of 117 tracks. Averages or sums of much data is required to get good spectra (Klymak & Moum 2007, a&b) so here when the authors start using smaller subsets of reflector tracks, it is necessary to show spectra sufficient to provide evidence their method is valid. The result of these adaptations is that the method used in this manuscript should be fully justified and show much supporting data.

We have made an effort to present our findings as clear and robust as we can, and interpreting the observed features based on these robust results. Concerning methodology, we essentially followed the indications of previously SO published works (e.g. Fortin et al. 2016; Holbrook et al., 2015) but adapting it to tracked reflectors within smaller windows. As suggested by the reviewer, and to clarify the main points of the procedure, we have added a more detailed, step-by-step description in the new version of the text:

The main steps of the procedure are the following ones: (1) Selecting a local window larger than the resolution of the data, but smaller than the entire seismic transect. The point is selecting the smallest possible window that allow calculating the reflector displacement spectra. We tested different window sizes and we found that the smallest ones that allow producing robust results are 1200 m wide x 15 m high. Results with larger windows are comparable in terms of amplitude and shape of the imaged features, but structures and boundaries are better defined with this window size (new Fig S1). (2) Calculating the spectra of all the reflectors inside the window (typically two to four for this window size) and average them. Examples of the results obtained for individual reflectors and average values obtained within different windows located in “high” and “low” mixing areas are shown in fig. 2rev 3 and new figure 6. Take the average value of the spectral amplitude between 13-30 m, which corresponds to the turbulent subrange (new Fig. S3). This range of scales can be resolved with the HR-MCS system used in this experiment, which has a theoretical lateral resolution of 8-17 m at the target depth (Sallares et al., 2016). (3) Applying Batchelor<sup>59</sup> relationship (equation 7) to retrieve mixing rate based on the turbulent spectral amplitudes obtained within each window, and then Osborn<sup>80</sup> (equation 1) to derive turbulent diffusivity from mixing rate. (4) As few tracked reflectors are included in the window, variances can affect the calculated diffusivities, then to eliminate this effect, we slide the window in small steps (30 m in horizontal and 3 in vertical direction), assigning the average value as explained above to every local window.

The analysis made for different window sizes and reflector lengths (new fig. S1) demonstrate the robustness of the results under different conditions and validate the procedure as a method to derive high-resolution turbulent diffusivity maps from MCS data.

A description of the procedure following steps 1-4 has been included in the new version of the m/s (lines 204-232).

We include in the new version of the manuscript a complementary analysis of reflectors recorded by our system. Besides, in figures 2rev. 2-3, we include much supporting data (windows and horizons analysis) that justify our findings in a robust way (new fig. 5-8, S1, lines 289-291; 301-305).

C) Many of the author's responses do not address the problems from the first review and the line numbers often point to incorrect sections of text. Specifically, here I am referring to the many times the line numbers refer to sections of text that are headers, blank lines, equations, or unchanged text [e.g. lines 100-102 (blank line in both manuscript versions and unchanged opening sentence); 162-165 (addition of sentence that doesn't add or address any concerns); 260-264 (only changed one word "anomalies" to "patches" which does not address the issues in the manuscript regarding k-rho values or distributions)]. The result is many changes that were difficult to track and, more importantly, often did not add to the clarity of the text or resolve the concerns posted in the prior review.

We apologize for having provided wrong number lines, we did not check it after the last edition of the previous version of the m/s. We have now checked that the comments and questions are addressed in the corresponding line numbers.

Lines 100-102 corresponded to lines 104-106. It refers to the method used to calculate the diapycnal mixing map.

Lines 162-165. We clarify and include the analysis of the 68 reflectors (figure 2rev1; new figure 2 and S3, lines 313-315) (Line 171-174), refers to the method used to obtain average dissipation rates.

Lines 260-264. It refers to the new window and horizon analysis that illustrates the relationship between shear instabilities and mixing hotspots (figure 2rev 3; new figure 5-8, lines 289-297).

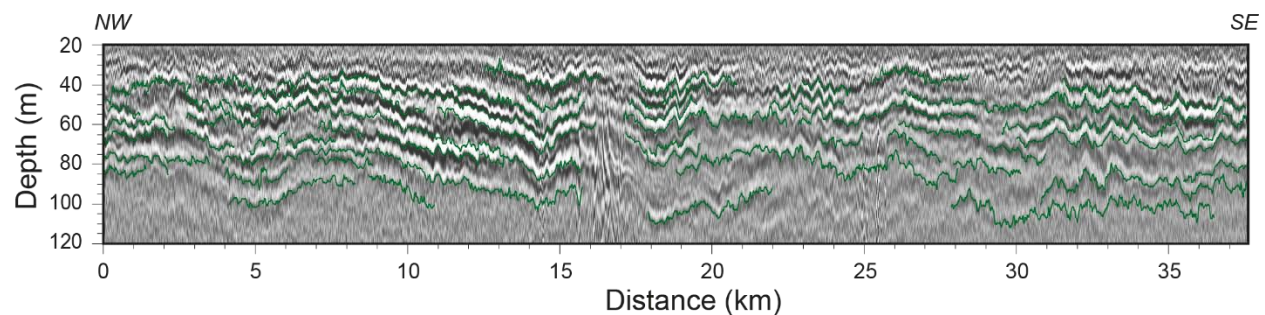


Figure. 2rev. 1. Depth-converted high-resolution multichannel seismic profile, with the tracked reflectors used in the spectral analysis superimposed (green lines).

#### Major Concerns:

D) Turbulence levels in Figure 6 do not match how H1, H2, and H3 are described in the

manuscript or how they fit into the turbulence map of figures 3 and 5. In the text and due to its location in figures 2 and 5, horizon H1 is described at the high turbulence reflector, while H2 and H3 are low and moderate. However, figure 6 shows the energy in the turbulent subrange of H1 to be significantly lower than either H2 or H3. The authors need to explain what is happening here or else how can we be sure their map of turbulence is accurate when the “high turbulence” example shows less energy in the turbulent subrange.

We agree that the individual horizons chosen in the previous version were not the most appropriate to illustrate the relationship between spectral amplitude and turbulence level. This is because the analysis to calculate the spectra is done for individual windows containing several reflectors (see description of the method above, as well as in lines 204-212), so the relevant value for the map is the average of all reflectors within the window. To be consistent with this and to illustrate better our approach, we have changed the reflector-based analysis of the previous version of the m/s for a window-based one in the new version (figs 2rev 2 and 3, and new figs. 5 and 6). Now we can see several examples of reflectors within 1200 m wide x 15 m high windows located in “high” and “low” mixing regions (W1 to W6 in fig 2rev 1 and new fig 5), showing window average displacement slope spectral values in the turbulent subrange that are above and below the Batchelor59 model, respectively. These are the values taken to construct the turbulent diffusivity map.

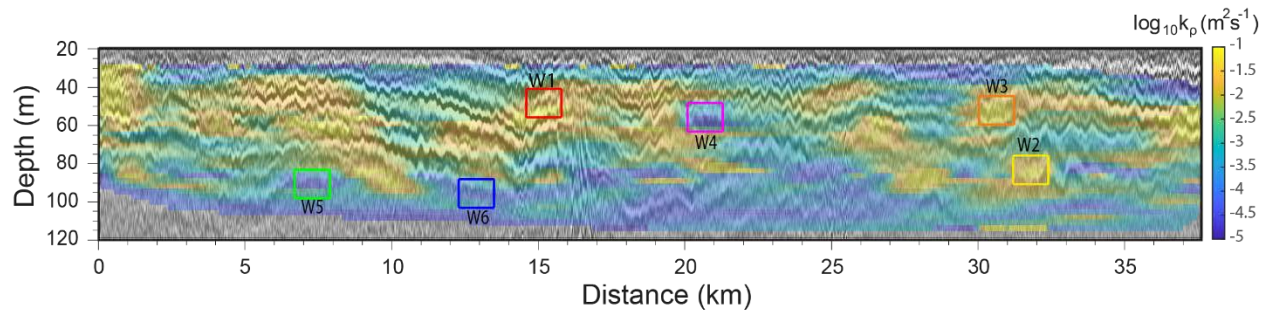


Figure 2rev. 2. High-resolution  $k_\rho(x, z)$  map overlapped with the HR-MCS image. Squares indicate location of some of the 1200 m x 15 m windows analyzed. They have been selected as examples of high-dissipation (windows W1-W3) and low-dissipation (windows W4-W6) areas. The color code of the squares is the same as for reflector spectra in figure 2rev. 3, so that colors coincide with those of displacement spectra within the corresponding window.

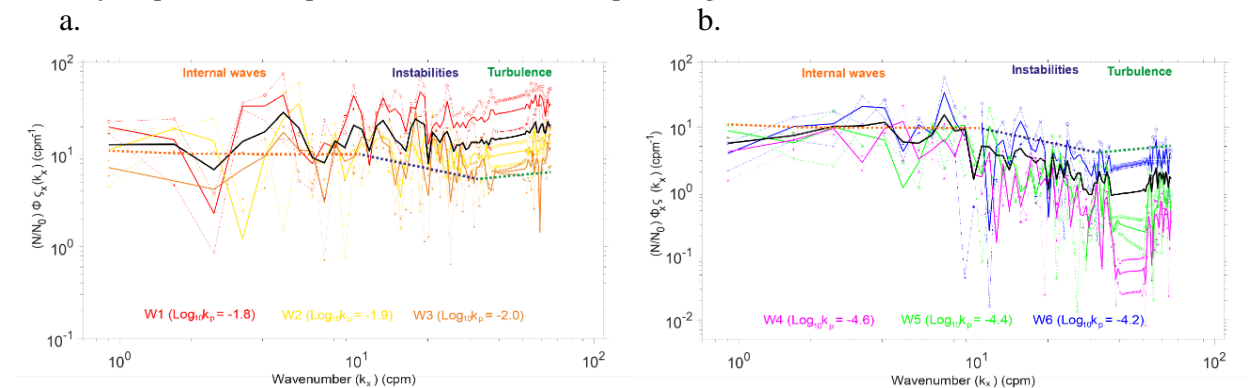


Figure 2rev. 3. Average horizontal spectrum of the vertical displacements of reflectors inside windows W1-W6 (see location and color code in figure 2rev. 2). (a) Spectra of individual reflectors in “high diffusivity” areas (thin dotted lines), average within windows W1 (red solid line), W2 (yellow solid line), and W3 (orange solid line), and average of the three “high diffusivity” windows (thick solid black line). (b) Spectrum of individual reflectors in “low diffusivity” areas (thin dotted lines), average within windows W4 (magenta solid line), W5 (green solid line), and W6 (blue solid line), and average of the three “low diffusivity” windows (thick solid black line). The reference lines are the theoretical slopes corresponding to the GM79 model for the internal wave subrange (brown dotted line), Kelvin-Helmholtz instabilities for the transitional subrange (dark blue dotted line), and Batchelor59 model for turbulence (dark green dotted line). Legend: Values of diapycnal diffusivity using spectral values at the turbulent subrange within each of the analyzed windows (same color code as for windows W1-W6).

We have included this window-based analysis in the new version of the manuscript to illustrate the energy variation in the different areas and the relation between the mixing level and the oceanic processes (section 3.3, lines 301-318).

E) There are issues with the representation of resolution of the method. As stated in the abstract (line 25), the authors claim to resolve mixing with a lateral resolution on the order of 10 meters. The method applied, a rolling 1200 m x 15 m analysis window, is attributing changes in spectral energy at the periphery of the window over half a kilometer away to the “high resolution” cell. It is unsurprising that, as stated in the conclusion (lines 397-398) the mixing hotspots appear to be 10-15 m vertically and 1-2 km laterally, a scale much closer to the real resolution of this treatment of the data. In their response the authors claim the method makes the turbulence maps appear more “realistic” and I agree that it does. The rolling window approach is not quite a smoothing function, but the authors should make certain the manuscript reflects the true resolution of the method.

We agree with the reviewer. The last sentence of the abstract was misleading so we have deleted it in the new version. It referred to the seismic system, not to the diffusivity map. As we explained in our previous response and was explained in the main text, the HR-MCS system has lateral resolution of  $O(10\text{m})$  (~12-15 m in our case), but the mixing map was created with 1200 wide x 15 high sliding windows, so this is the approximate resolution of the map itself. We have emphasized this in the new version of the m/s (line 82-84 and 204-213).

F) Figures that are necessary, and have been produced by the authors, are missing from the manuscript.

- Figure rev2-3 shows the tracks of all the reflectors and detail of spatial coverage. This figure adds emphasis that a rolling window approach is potentially viable for this seismic line and a table or at least an average number of tracks per analysis window would make an excellent addition and help justify the handling of the data as was done in the manuscript.

Done, we include the figure in the main text (new Fig. 2), and the data requested in the manuscript (line 218-220).

- Figure rev2-2 shows much needed support for how the data was handled. The gray lines on this figure are hard to compare but show considerable variability. A re-working of this type of figure would give indication to just how certain we can be about analyses of a small number of reflector tracks broken into ~1-2 km segments.

Done, we include the figure 2rev. 3 in the main text (new Fig. 6).

- Figures rev2-5, rev2-6, rev2-7 include the turbulent subrange. This manuscript is fundamentally about turbulence and parts “d” from these figures should be included.

Done, we include the turbulence figures in the manuscript (new Fig. 7, and 8)

G) The relationship between internal waves and turbulence is still somewhat unclear. Lines 20-21 state “mixing tends to concentrate in areas where internal wave[s] become unstable and shear instabilities develop.” This statement leads readers to think the data have a noted relationship between internal wave and turbulent structures. However, in the conclusion lines 406-407 say, “we found no clear correspondence between the location of the mixing patches and the location and amplitude of IWs” (also lines 255-256) then go on to discuss a relationship between shear instability and mixing. These two statements seem to be at odds with one another. The matter is further confused by introducing the relationship with shear instability. This reads as saying that (1) IWs and shear instability are related, (2) shear instability and turbulence are related, but (3) IWs and turbulence are not related. If both IWs and turbulence are related to shear instability, then it should follow that a relationship between IWs and turbulence would also exist.

Thanks for the comment. We agree that this deserves a clarification. As we mentioned above, we do not mean that there is no relationship between IWs and mixing. What we mean is that mixing increases in areas where IW instabilities develop. We interpret this as a sign that the development of shear instabilities is a mechanism that enhance energy transfer between IWs and turbulence. We hope this is now clearer in the new version (lines 19-22, 380-381, 441-447).

H) I am confused about the changes reported about analysis window length for figure 7a. Per previous review suggesting an analysis window of 1.2 km (to match the mapping analysis) the text was updated to say that figure 7a was done at 1.2 km in place of the first version using a 1 km window. However, this is no change in figure 7a from the previous version of the manuscript. I would expect a smoother profile of k-rho, particularly since the addition of 0.2 km is quite significant at the plotted scale and would encompass entire spikes and drops in turbulent signature. Further, figure rev2-2 shows great variability in non-overlapping 1.6 km segments, so there are significant differences at different points in the line and there should be differences when showing sliding 1.2 km segments as compared to 1 km segments.

Thank you. We rechecked the figures and now we include the ones with an analysis window length of 1.2 km. This way we get a smoother profile, and a clearer turbulence signature (new figure 7-8).

## I) Minor Concerns

Please explain the scale factor “b” (line 182)

Done (Line 188).

Here we shown the marked-up manuscript version:

## High-resolution diapycnal mixing map of the Alboran Sea thermocline from seismic reflection images

Jhon F. Mojica<sup>1,2</sup>, Valentí Sallarès<sup>2</sup>Sallarès<sup>2</sup>, Berta Biescas<sup>2,3</sup>

<sup>1</sup> Center for ~~Global~~global Sea Level Change CSLC – NYUAD, Abu Dhabi UAE.

<sup>2</sup> Institute of Marine Sciences, ICM-CSIC, Barcelona, Spain

<sup>3</sup> Consiglio Nazionale delle Ricerche CNR-ISMAR, Bologna, Italy

10 *Correspondence to:* Jhon F. Mojica (~~jfm11@nyu.edu~~)jhon.mojica@nyu.edu

**Abstract.** The Alboran Sea is a dynamically active region where the salty and warm Mediterranean water first encounters the incoming milder and cooler Atlantic water. The interaction between these two water masses originates a set of sub-mesoscale structures and a complex sequence of processes that entail mixing close to the thermocline. Here we present a high-resolution map of the diapycnal diffusivity around the thermocline depth obtained using acoustic data recorded with a high-resolution multichannel seismic system. The map reveals a patchy thermocline, with ~~areas~~spots of strong diapycnal mixing juxtaposed with ~~others~~areas of weaker mixing. The patch size is of a few ~~km~~kms in the horizontal scale and of 10-15 m in the vertical one. The comparison of the obtained maps with the original acoustic images shows that mixing tends to concentrate in areas where internal ~~wave~~waves, which are ubiquitous in the surveyed area, become unstable and shear instabilities develop, enhancing energy transfer towards the turbulent regime. These results are also compared with others obtained using more conventional oceanographic probes. The values estimated based on the seismic data are within the ranges of values obtained from oceanographic data analysis, and they are also consistent with reference theoretical values. Overall, our results demonstrate that high-resolution seismic systems allow to remotely quantifyquantifying mixing at the thermocline depth with a lateral unprecedented resolution of  $O(10^1\text{ m})$ .

KEYWORDS: Thermocline mixing, Seismic Oceanography, Diapycnal ~~diffusivity~~mixing map.

### 30 1. INTRODUCTION

Diapycnal diffusivity ( $k_p$ ) around the thermocline plays a major role to control the strength and pattern of the ocean circulation, because it determines heat and salt heterogeneity at different spatial scales. This process usually occurs in a vertically stratified regime, affecting adjacent layers with the same density but different temperature and salinity (Stewart, 2008). In terms of processes, mixing in the ocean can be separated in two categories. One ~~is related~~corresponds to internal wave (IW) breaking, which produces turbulent motion and changes the density stratification, while the second concerns the development of high frequency dynamic instabilities that are formed due to shear (Gregg, 1987; D'Asaro and Lien, 2000). As the spatial scale decreases, mixing leads to an unbalanced pressure field that eventually results in a collapse and dispersion of mixing waters through isopycnals (Thorpe, 2005). The value of  $k_p$  depends on the buoyancy frequency ( $N$ ) and the dissipation rate ( $\epsilon$ ) as indicated by the so-called Osborn (1980) relationship:

$$k_p = \Gamma\epsilon/N^2 \quad (1)$$

Style Definition: Comment Text

Formatted: Font: 12 pt

Formatted: Font: Times New Roman

Formatted: Font: Times New Roman



This value, where  $\Gamma = 0.2$  is the empirically defined mixing efficiency (Osborn and Cox, 1972), corresponds to the mixing between isopycnal layers in the thermocline. The global mean  $k_\rho$  value is of the order of  $10^{-4} m^2 s^{-1}$  (Munk and Wunsch, 1998), which corresponds to the value required to keep overturning in the thermocline. It has been shown that if  $k_\rho \ll 10^{-5} m^2 s^{-1}$  ~~there, the energy~~ is not enough ~~energy~~ to generate mixing (Gregg, 1989).

Formatted: Font: Times New Roman

Formatted: Font: Times New Roman

In a conservative flow,  $\varepsilon$  might present small variation due to dissipated heat through turbulent motions, but in the presence of strong shear,  $\varepsilon$  tends to increase (Thorpe, 2005), reaching a maximum value close to the Kolmogorov scale (Gargett and Holloway, 1984). Good knowledge of its behavior provides important clues on available energy and its transfer between spatial scales.

The loss rate of kinetic energy in the turbulent motion is commonly expressed as:

$$\varepsilon = \left(\frac{\nu}{2}\right) \langle S_{ij} S_{ij} \rangle \quad (2)$$

$$S_{ij} = \left(\frac{\partial u_i}{\partial x_j} + \frac{\partial u_j}{\partial x_i}\right) \quad (3)$$

Where  $\nu = 1.064 \times 10^{-6} m^2 s^{-1}$  is the kinematic viscosity and the tensor  $S_{ij}$  is a function of the velocity components in the three orthogonal directions (Thorpe, 2005). Conventional in-situ techniques as Vertical Microstructure turbulence Profiler (VMP) or microriders provide the most accurate measures of  $k_\rho$ , but in just one dimension. In general, although measures are accurate in the vertical dimension, sampling in the horizontal direction is much poorer, particularly in the  $\sim 10^3 - 10^4 m$  range (Klymak and Moum, 2007 a, b). Since this is the range of scales at which the transition between isotropic internal wave and anisotropic ~~turbulence motion~~ turbulent motions (i.e. mixing) occurs, the observational evidence of mixing patterns and the understanding of the underlying physical mechanisms are rather limited so far. Overall, direct measures and observations are too few to create a global mixing map with the required resolution to feed the models with ~~appropriate~~ proper values of dissipation ~~ranges~~ rates (Smyth et al., 2011). This makes ~~it~~ in turn ~~it~~ difficult to integrate mixing into large-scale ~~models of~~ ocean dynamics ~~models~~. Its effects are simulated instead through the incorporation of eddy diffusivity coefficients, which are tuned *ad hoc* to match the large-scale distribution of ocean observables. While this approach allows to properly reproduce regional spatial-temporal patterns, it severely hampers the long-term predictive capability of ocean dynamics and, in turn, that of climate models. Improving our knowledge on the short-term and small-scale mixing mechanisms and integrating them into large-scale models remain thus as an outstanding challenge.

Formatted: Font: Times New Roman

To overcome this issue, remote sensing techniques have recently started to be used (e.g. Gibson et al., 2007). One of these alternative techniques is multichannel seismics (MCS), an acoustic method providing quasi-synoptic images of the thermohaline boundaries in the ocean interior to full ocean depth, with a lateral resolution of ~~up to~~  $O(10^4 m)$  (Holbrook et al., 2003). Several recent works have demonstrated that it is actually possible to map  $k_\rho$  using measures of the horizontal wavenumber ( $k_x$ ) spectra of the vertical displacements of thermohaline boundaries imaged with MCS acquisition systems (Sheen et al., 2009; Holbrook et al., 2013; Fortin et al., 2016). However,

Formatted: Font: Not Italic

Formatted: Font: Times New Roman

these studies use conventional, relatively low-resolution systems with source energy concentrating below  $\sim 50$  Hz. In addition, ~~these~~ due to the long wavelength source wavelet, conventional MCS systems are not well suited to image the shallowest ocean layers (i.e.  $< 200$  m), but deeper water levels ( $\rightarrow$   $> 400$  m depth). At these depth levels, ~~the~~ changes in the internal structure are usually less marked than ~~those~~ at shallower levels, ~~and~~ especially around the thermocline. In a recent work, it has been shown that portable, high resolution MCS (HR-MCS) systems, which use a smaller energy, but higher-frequency source, ( $> 150$  Hz), allow imaging the thermohaline structure as shallow as  $\sim 30$  m with a lateral resolution of  $12-15$  m and ~~1-2 m in the~~ vertical ~~direction~~ one of 1-2 m (Sallares et al., 2016). This resolution is three- to four-fold better than that of conventional MCS systems that have been used to image deeper ocean levels. Therefore, it has the potential to image sub-mesoscale structures and processes that affect the thermocline at scales of kilometers to tens of meters, allowing ~~to cover~~ covering the existing observational gap. Despite its potential, HR-MCS systems have never been used to date to quantify diapycnal mixing at the thermocline depth.

Here we use the above-mentioned method of extracting  $k_p(x, z)$  maps from MCS images, but applied for the first time to HR-MCS data acquired in the Alboran Sea (Westernmost Mediterranean). The method to calculate diapycnal mixing maps from the horizontal wavenumber spectra of vertical reflector displacements is ~~analogous to~~ based on that proposed by Sheen et al. (2009) and Holbrook et al. (2013). The result is a high-resolution mixing map of the ocean at the thermocline depth ( $30-110$  m) along a  $35$  km-long transect (Fig. 1a). This method ~~can~~ could be ~~used~~ applied in other regions where the shallow water ~~column is~~ levels are sufficiently stratified to ~~record~~ allow recording the reflected energy at the acoustic impedance variations (density x sound speed contrasts between neighboring water layers).

The rest of the manuscript is structured as follows: in section 2 we present the hydrographic context; and the observations; then we describe the acquisition system and the method applied to estimate  $k_p$  from the seismic data. The results are described in section 3, whereas the discussion about the imaged structures and their likely causes is presented in section 4. Finally, section 5 summarizes the main conclusions.

## 2. DATA AND METHODOLOGY

The Alboran Sea is characterized by the continuous exchange between Mediterranean Water (MW) and Atlantic Water (AW) through the Strait of Gibraltar. This exchange concentrates near the surface (between  $\sim 30$  m and  $\sim 200$  m); where the shallow, moderately ~~saline~~ saline and cold incoming AW ( $< 50$  m) interacts with the deeper, warmer, saltier and more stable outgoing MW, producing another water mass known as Modified Atlantic Water (MAW). In this framework, internal waves, strong horizontal shear instability, and prominent thermohaline stratification are generated. These particular features reflect the complex dynamic setting of the area, with kinetic energy being transferred between isopycnals from large to small scales, leading eventually to overturning, isotropic turbulence and irreversible mixing.

The data set used in this work, which includes collocated seismic and oceanographic measurements, was collected on board the Spanish R/V Hesperides in the framework of the IMPULS-2006 experiment. Here, we concentrate our analysis on one of the seismic profiles

Formatted: Font: Times New Roman

Formatted: Font: Times New Roman

Formatted: Font: Italic



of isopycnals, is small in the surveyed area ( $\approx 1$ ), we assume that the assumptions and approximations of the model are valid, so it is not necessary to consider alternative ones such as the one presented in Waterman et al. (2013). The Gregg89 model is commonly applied in the mid-latitude thermocline, linking shear current at different depths. The simplest way to obtain average dissipation rates over large space and time scales is through:

$$\varepsilon = 7 \times 10^{-10} N^2 / N_0^2 < S_{10}^4 / S_{GM}^4 > \quad (4)$$

$$S_{10}^4 = 4.22 [(\Delta U / \Delta z)^2 + (\Delta V / \Delta z)^2]^2 \quad (5)$$

$$S_{GM}^4 = 2 \left[ \frac{(3\pi/2) j_x E_{GM} b N_0^2 k_x^c (N/N_0)^2}{(3\pi/2) j_x E_{GM} b N_0^2 k_x^c (N/N_0)^2} \right]^2 \quad (6)$$

Where  $N_0 = 5.2 \times 10^{-3} \text{ s}^{-1}$  is the reference buoyancy frequency,  $S_{10}$  is the shear variance calculated from the meridional ( $V$ ) and zonal ( $U$ ) velocity variations according to the as a function of depth ( $z$ ),  $S_{GM}$  is the variance for the Garret-Munk model (Gregg, 1989),  $j_x$  is a mode number,  $E_{GM}$  is the Garrett-Munk energy density,  $b$  is the scale factor,  $c$  is the spectrum slope, and  $k_x$  is the horizontal wavenumber.

Alternatively, the model proposed by Batchelor (1959); hereafter referred to as Batchelor59, estimates  $k_p$  as a function of the energy transfer from large to small scales in the turbulent regime. This model assumes that the energy exchange from mechanical to caloric due to  $N$  and  $\varepsilon$  can be approximated as:

$$\varphi_\zeta^T = \left( \frac{4\pi\Gamma}{N^2} \right) C_T \varepsilon_T^{2/3} (2\pi k)^{-5/3} (2\pi k_x)^{-5/3} \quad (7)$$

Where  $\varphi_\zeta$  is the energy spectrum of the isopycnals vertical displacement measured in the turbulent subrange; and  $C_T$  is a proportionality constant (Sreenivasan, 1996). We apply this model to estimate the mixing rates over the seismic profiles, applying a method proposed and described in previous works, (e.g. Sheen et al., 2009; Holbrook et al., 2013). The main steps of this approach and the specifics of our work are described below.

To identify (1) Selecting a local window larger than the dissipation signature in the resolution of the data, but smaller than the entire seismic profile, transect. The point is selecting the smallest possible window that allows to properly calculating the reflector displacement spectra. We tested different window sizes and we found that the smallest ones that allow producing robust results are 1200 m wide x 15 m high. Results with larger windows are comparable in terms of amplitude and shape of the imaged features, but structures and boundaries are better defined with this window size (Fig. S1). Smaller windows contain too few reflectors and produce abundant artefacts. Longer tracks are cut into shorter segments to fit inside the window. As it is explained in Sallares et al. first calculate (2016) and shown in Fig. S2, this does not affect the spectral values at the spatial scale range analyzed.

Formatted: Font: Times New Roman

Formatted: Font color: Custom Color(RGB(0,0,10))

Formatted: Font: Times New Roman

Formatted: Font: Times New Roman

Formatted: Font: Times New Roman

Formatted: Font: Times New Roman

230 (2) Computing the energy level of the displacement spectra in the turbulent subrange from our data by averaging the value obtained for all the reflectors within 1200 m wide and 15 m high windows. Longer tracks are cut to fit inside the window, and calculate. As it is explained in Salares et al. (2016), this does not affect the average spectrum at the spatial scale range analyzed. We then apply. The spectral subranges observed in the combined spectrum of the 68 reflectors (Fig. S3), which are also observed in most individual windows and reflectors, are used as a reference to select the scale range to compute the spectral amplitudes. In the case of the turbulent subrange, it is 13-30 m. The mean number of reflectors fitting inside the 1200 m wide x 15 m high windows is three, ranging from two to four depending on the imaged area.

Formatted: Font: Times New Roman  
Formatted: Font: Times New Roman  
Formatted: Font: Times New Roman  
Formatted: Font: Times New Roman  
Formatted: Font: Times New Roman  
Formatted: Font: Times New Roman  
Formatted: Font: Times New Roman

240 (3) Applying the Batchelor59 model, (Eq. (7)), to estimate  $\epsilon_z$ , using the obtained turbulent energy level (i.e. the average  $\phi_\zeta$  between 13-30 m) computed within the window (transitional subrange), with  $I=0.2$ ,  $C_T=0.3$ , and  $N$  is calculated according to depth. Finally, we apply Osborn80 relationship (Eq. (1)) using the  $\epsilon_z(x, z)$  values obtained above to estimate compute  $k_\rho(x, z)$ . These

Formatted: Font: Times New Roman

245 (4) As only few tracked reflectors are included inside each window, variances can affect the calculated diffusivities. To mitigate this effect, we slide the window in small steps are repeated within windows of the size mentioned above that slide 30 m in the (30 m in horizontal direction and 3 m in the vertical at each new analyzing step direction), assigning the average value of the spectral amplitude to each local window. The fact that we incorporate few new data at each step, produces a smoothly varying map with a resolution that is similar to the window size (~1000x10 m), instead of the one with sharp bounds/boundaries that would be obtained without using overlapping windows (e.g. Sheen et al., 2009; Holbrook et al., 2013 Fig. S1).

Formatted: Font: Not Italic

255 In summary, both on one hand we apply the Gregg89 and model to obtain a vertical  $k_\rho(z)$  profile using the XCTD and ADCP data, and on the other hand we apply Batchelor59 models are used to estimate mixing rates from two independent data sets: XCTD ADCP and seismic data, respectively obtain a  $k_\rho(x, z)$  map using the vertical displacement spectra of the tracked reflectors. The results obtained using both methods and models are then compared to check if they are consistent, and to gain confidence in the proposed HR-MCS methodology. We then analyze and discuss the high-resolution 2D map resulting from the seismic data maps in terms of mixing.

260

### 3. RESULTS

265 The procedure described above allowed producing a smoothly varying  $k_\rho(x, z)$  map that covers the whole profile (Fig. 3) were obtained applying the sliding window approach explained above. The goal is being able to identify features and processes occurring in the transition between the internal wave and the turbulence sub-regimes/subranges, such as the intensity and scales of variability of the mixing patches, the location and size of the hotspots/mixing patches and their potential relationship with oceanographic features such as IWs or shear wave instabilities. For this, we also use the vertical  $k_\rho(z)$  profile obtained from the XCTD and ADCP (Fig. 4a).

Formatted: Font: Times New Roman  
Formatted: Font: Italic

270

#### 3.1. Probe-based $k_\rho(z)$ profile

Formatted: Font: Times New Roman

As we mentioned above, to have a reference value to compare with the MCS-based  $k_\rho(x, z)$  maps, we have first calculated a  $k_\rho(z)$  profile for shallow waters ( $< 200\text{ m}$ ) using the XCTD and ADCP data and applying the Gregg89 model (Eqs. 4-6). To do this we have used ADCP measures averaged within 10 m-depth bins. By doing this, we obtain an average value for the shear variance of  $S_{10}^4 = 0.28\text{ s}^{-4}$ , whereas the reference value of the shear variance obtained from the Garrett-Munk model (Gregg, 1989) is  $S_{GM}^4 = 0.013\text{ s}^{-4}$ . This gives an average dissipation rate  $\langle \varepsilon \rangle \approx 1.3 \times 10^{-8}\text{ Wkg}^{-1}$ , and an average diapycnal diffusivity  $\langle k_p \rangle \approx k_\rho \approx 10^{-3.0}\text{ m}^2\text{ s}^{-1}$  for the targeted depth range (Fig. 4a). The  $k_\rho(z)$  profile obtained from the XCTD and ADCP is also shown in Fig. 4a, together with the global averages for overturning ( $\langle k_\rho \rangle \approx 10^{-4}\text{ m}^2\text{ s}^{-1}$ ) as well as the average pelagic diffusivity in the ocean ( $\langle k_\rho \rangle \approx 10^{-5}\text{ m}^2\text{ s}^{-1}$ ).

We obtain minimum values of the mixing rate at 50-55 m, 68-73 m, and 100-125 m. The absolute minimum of  $k_p = k_\rho = 10^{-5.2}\text{ m}^2\text{ s}^{-1}$  is obtained at  $\sim 115\text{ m}$ , whereas the maximum is of  $10^{-2.1}\text{ m}^2\text{ s}^{-1}$  at  $\sim 15\text{ m}$ . This gives a range of variation of  $10^{-3.1}\text{ m}^2\text{ s}^{-1}$ . Deeper than this, the mixing variability is smaller. The Turner angle and buoyancy frequency (Fig. 4b) indicate that the region is mostly stable with a slight tendency to double-diffusion ( $Tu \sim 45^\circ$ ).

It is worth noting that, at this specific location, the average vertical  $\varepsilon(z)$  and  $k_\rho(z)$  values are one order of magnitude higher than the global average ones. The higher values probably reflect the effect of overturning in the thermocline. While probe-based measurements are well suited to investigate mixing variability in the vertical dimension, they do not provide information on the variability in the horizontal dimension with a comparable level of detail. As explained above, to do this we have used estimations of  $\varepsilon$  and  $k_p, k_\rho$  based on the HR-MCS data, but applying Batchelor59 model (Eq. 7) in this case instead.

### 3.2. High-resolution multichannel seismic-based $k_\rho(x, z)$ map

The  $k_\rho(x, z)$  map displayed in Fig. 3 has average values of  $\langle \varepsilon \rangle \approx 6.5 \times 10^{-9}\text{ Wkg}^{-1}$  and  $\langle k_p \rangle \approx k_\rho \approx 10^{-2.7}\text{ m}^2\text{ s}^{-1}$ . These values are within the range of values obtained from the XCTD and ADCP data but, at the same time, they are over an order of magnitude higher than the global ocean reference value of  $k_p = k_\rho \approx 10^{-4.0}\text{ m}^2\text{ s}^{-1}$  (Fig. 4a). Figure 5 displays the  $k_\rho(x, z)$  map superimposed with the HR-MCS data. It is interesting to note that the range of horizontal variability is similar to that observed in the vertical dimension, although there is no direct visual correspondence between the  $k_p, k_\rho$  anomalies and IWs. The range of variability is of over three orders of magnitude, locally reaching an extreme value of  $k_p, k_\rho \approx 10^{-1.5}\text{ m}^2\text{ s}^{-1}$  at a depth of  $\sim 55\text{ m}$  and at  $16\text{ km}$  along the line; and a minimum value of  $k_p, k_\rho \approx 10^{-4.5}\text{ m}^2\text{ s}^{-1}$  at  $\sim 95\text{ m}$  depth and  $20\text{ km}$  along the line, which is close to the global oceanic average.

To better illustrate the procedure followed to generate the maps, several examples of  $k_\rho$  values obtained in “high” and “low” mixing areas, and the corresponding window average of the computed displacement spectra, are shown in Fig. 6. Numerous patches with  $k_p, k_\rho$  values exceeding  $10^{-2}\text{ m}^2\text{ s}^{-1}$ , with a characteristic size of 1-2 km in the horizontal dimension and  $\sim 10\text{ m}$  in the vertical are found throughout the whole section (i.e., the yellowish patches in Figs. 3 and 5). Not only the average depth value, but also the vertical size of the anomalies, as well as the range of  $k_p, k_\rho$  variation, are in agreement with the probe-based values (Fig. 4). The contribution of the high

Formatted: Font: Times New Roman

Formatted: Font: Times New Roman

Formatted: Font: 12 pt

Formatted: Font color: Auto

Formatted: Font: Times New Roman, Font color: Auto

Formatted: Font color: Auto

Formatted: Font: Times New Roman, Font color: Auto

Formatted: Font: Times New Roman, 12 pt

Formatted: Font: Times New Roman

Formatted: Font: Times New Roman

Formatted: Font: Times New Roman

Formatted: Font: Times New Roman

Formatted: Font: Italic

$k_p/k_\rho$  patches to the local average value is therefore outstanding, raising it from a background average value of  $\sim 10^{-4} \text{ m}^2 \text{ s}^{-1}$  to  $\sim 10^{-2.5} \text{ m}^2 \text{ s}^{-1}$ .

320

To try to understand the existing relationships between mixing variability and water dynamics, we analyze various reflectors to identify a possible visual correspondence between individual sub-mesoscale features and mixing hotspots. Among the numerous horizons examined, we show in fig. 5, three horizons named H1, H2, H3, which spatially coincide with anomalously high and low mixing patches. For these three horizons, we have analyzed the structures observed in the different sub-regimes.

325

### 3.3 Analysis of individual reflectors

H1 is located at  $\sim 50 \text{ m}$  depth and has a length of  $\sim 5.5 \text{ km}$  ( $31.5\text{--}37 \text{ km}$  along profile). It was selected because it is laterally coherent for several kms and, it coincides with one of the high **3.3 Correspondence between mixing hotspots and imaged oceanographic features**

330

To discuss the possible origin, or nature, of the mixing hotspots identified in the  $k_\rho(x,z)$  map (Fig. 5). Its corresponding  $k_x$  spectrum is displayed in Fig. 6a.

335

3), we have visually compared the lateral variation of diapycnal diffusivity, with the structures imaged at the different subranges, along several individual reflectors. The analyzed reflectors have been selected as examples of high diffusivity (H1 and H2 in Fig. 7) and low diffusivity (H3 and H4 in Fig. 8) areas. To calculate  $k_\rho$  over the whole ( $x$ ) along each horizon (Fig. 7a) we used have computed the spectral energy obtained within a  $1.2 \text{ km}$ -wide window moving laterally  $30 \text{ m}$  at each step along the whole profile reflector. To analyze the features that contribute to the energy spectrum in the different scales, and to compare them in turn with the  $k_x$  values obtained along the entire reflector length, the horizon has  $k_\rho(x)$ , the horizons have been filtered at wavelength bands the scale ranges attributed to the IW subrange ( $3000\text{--}100 \text{ m}$ ), and the instability dominated subrange ( $100\text{--}30 \text{ m}$ , transitional subrange) ( $100\text{--}30 \text{ m}$ ), and turbulent ( $30\text{--}13 \text{ m}$ ) subranges, respectively. As a reference, the local horizontal buoyancy wavelength, estimated from the XCTD data is  $\lambda_N \sim 90 \text{ m}$  (Sallares et al., 2016). The different spectral subranges that are observed in the combined spectrum of the 68 reflectors (fig. S1) is also observed in most individual. Although no general conclusions should be extracted from the analysis of a few individual reflectors, they show some relevant trends and correspondences to be taken into account when interpreting the results. In this sense, a clear trend that is observed in the displacement spectra such as those displayed in fig. 6. One of the main features is the systematic steep slope spectra obtained at the instability dominated subrange, which is likely associated with the loss of energy in the wave field due to dissipation (e.g. transitional subrange between IWs and turbulence (Fig. S3), Samodurov et al., 1995). As it is explained in Sallares et al. (2016), the variation of the slope spectra at the intermediate scale this slope is consistent with numerical estimates for the evolutionary stage of the vortex sheet linked to shear instabilities (Waite, 2011), and it likely reflects the loss of energy in the wave field due to dissipation (e.g. Samodurov et al., 1995).

340

345

350

355

360

Regarding horizons crossing high dissipation areas (H1 and H2 in Fig. 7), a striking feature is the notable, sudden decrease in correspondence between the amplitude of the vertical displacements imaged in the transitional subrange and the variation in  $k_\rho$ . Hence, a variation in the amplitude of the features observed in the transitional subrange, at  $\sim 34.7 \text{ km}$  along the profile (red

Formatted: Font: Times New Roman

dashed line in Fig. 7). Interestingly, a change in the  $k_p$  value is also observed at this point. Left of it (31.5–34.7 km along profile), H2 (red lines in Fig. 7a), coincide with a decrease in  $k_p$ . In the case of H1, the average  $k_p$  value to the left of this point is  $10^{-2.5} \text{ m}^2 \text{ s}^{-1}$ , while right of this point (34.7–37 km), it is  $10^{-3.0} \text{ m}^2 \text{ s}^{-1}$ . Although both, whereas in the case of H2, the average  $k_p$  value to the left of this point is  $10^{-4.1} \text{ m}^2 \text{ s}^{-1}$ , while right of this point, it is  $10^{-2.9} \text{ m}^2 \text{ s}^{-1}$ . Although most of these values are higher than the average global value for meridional overturning circulation, the highest local average values are obtained in the region where the clearest, largest amplitude features, possibly representing KH billows (Sallares et al., 2016), are imaged. Conversely, there is no clear visual correlation between internal wave attributes and  $k_p$  variations.

H2 is located at  $\sim 95 \text{ m}$  depth and has a length of  $\sim 4.0 \text{ km}$  (18–22 km along profile). It was selected because its location coincides with a relatively weak mixing area, according to the  $k_p$  map (Fig. 5). The corresponding  $k_x$  spectrum is shown in Fig. 6b. As in the previous case, we have first calculated  $k_p$  using the spectral energy values within 1 km wide window, moving laterally 30 m at each step, along the whole reflector length. The average value for the whole horizon is  $k_p \sim 10^{-4.4} \text{ m}^2 \text{ s}^{-1}$ , so considerably lower than in H1 but close to the global average value. We have subsequently filtered H2 at the IW (3000–100 m) and transitional (100–30 m) sub ranges and compared it with the obtained  $k_p$  values (Fig. 8). In this case, we have identified three different segments as a function of their average  $k_p$  value. The first and third segments (18–19.6 km and 20.4–22 km, respectively) display average  $k_p$  values that coincide, within error bounds, with those of the global ocean average. In particular, we obtain  $k_p \sim 10^{-4.0} \text{ m}^2 \text{ s}^{-1}$ , for the first segment, and  $k_p \sim 10^{-3.8} \text{ m}^2 \text{ s}^{-1}$ , for the third one. The second or breaking segment, instead, displays a value of  $k_p \sim 10^{-4.8} \text{ m}^2 \text{ s}^{-1}$ , which is well below the global ocean average.

H3 is located at  $\sim 80 \text{ m}$  depth and has a length of  $\sim 12 \text{ km}$  (3.5–15.5 km along profile). It was selected because its location pass through low and high mixing areas, according to the  $k_p$  map (Fig. 5). The  $k_p$  values along the profile have been calculated following the same approach as for the other two reflectors. Its corresponding  $k_x$  spectrum is displayed in Fig. 6c. As in the case of H1, While we can identify a clear visual correspondence of high mixing values and the largest-amplitude features imaged in the transitional subrange, but not with IWs. Between 9 km and 15.5 km along the profile the average  $k_p$  value is  $10^{-2.7} \text{ m}^2 \text{ s}^{-1}$ , while at the left of it (4–9 km along profile) it is  $10^{-4.8} \text{ m}^2 \text{ s}^{-1}$ . The situation is therefore very similar to the case of H1, and the same correspondence is also observed for the other reflectors along the profile, especially for those located in high mixing areas. no direct correspondence is found with specific IWs, which are ubiquitous all along the profile.

For the low dissipation areas (Fig. 8), we have selected H3, which is located at  $\sim 35 \text{ m}$  depth and has a length of  $\sim 3.5 \text{ km}$  (17.5–21 km along profile), and H4, located at  $\sim 95 \text{ m}$  depth and  $\sim 4.0 \text{ km}$  long (32.5–36.5 km along profile). They were selected because their location coincides with a relatively weak mixing area, according to the  $k_p(x, z)$  map (Fig. 8a). As in the previous case, we have first calculated  $k_p$  using the spectral energy values within 1.2 km-wide window, moving laterally 30 m at each step, along the whole reflector length. In the case of H3, the average value for the whole horizon is  $k_p \sim 10^{-4.2} \text{ m}^2 \text{ s}^{-1}$ , so considerably lower than in H1 but close to the global average value, whereas for H4, it is  $k_p \sim 10^{-4.1} \text{ m}^2 \text{ s}^{-1}$ . In this case, we have identified some peaks at the transitional subrange that coincide with local highs in  $k_p(x)$ . The peaks in H3 (at 18.4 km, 19.3 km, 19.9 km and 20.4 km) and in H4 (at 33.5 km, 34.9 km, 35.3 km, and 35.8 km) display average



410  $k_p$  values that coincide, within error bounds, with those of the global ocean average. In particular,  
we obtain  $k_p \approx 10^{-3.1} m^2 s^{-1}$ ,  $k_p \approx 10^{-3.3} m^2 s^{-1}$ ,  $k_p \approx 10^{-3.4} m^2 s^{-1}$ , and  $k_p \approx 10^{-3.5} m^2 s^{-1}$ , respectively, for  
each peak in H3, and  $k_p \approx 10^{-3.0} m^2 s^{-1}$ ,  $k_p \approx 10^{-3.2} m^2 s^{-1}$ ,  $k_p \approx 10^{-3.1} m^2 s^{-1}$ , and  $k_p \approx 10^{-2.9} m^2 s^{-1}$ ,  
415 respectively, for each peak in H4. There are four more peaks at 19.5 km and 20.1 km in H3 and 34  
km and 36.3 km in H4 that show no visual correspondence with structures in the transitional  
subrange but with larger amplitude features in the turbulent subrange, so we hypothesize that they  
could be related to smaller-scale turbulent processes. The segments with no direct visual  
correspondence with  $k_p$  peaks, instead, display average  $k_p \approx 10^{-4.3} m^2 s^{-1}$ , which is close to the global  
ocean average (Fig. 4a).

#### 4. DISCUSSION

420 The spatial variability observed along isopycnals based on the spectral analysis of the seismic data  
allows identifying a number of local features at different evolutionary stages. These features are  
the manifestation of relevant oceanographic processes and structures, such as IWs at the internal  
wave sub-range waves in the IW subrange, hydrodynamic instabilities at in the transitional sub-  
425 range subrange, and turbulence at smaller scales. These processes are likely responsible of the disruption of the  
finest structure in the seismic image, and the high amplitude variability or disappearance of some seismic  
reflectors.

The large variations observed in the  $k_p$  vertical( $z$ ) profile (Fig. 24), together with the slight tendency  
430 to double-diffusion identified in the Turner angle, suggest that the system is prone to be affected  
by advection processes (e.g. Kunze and Sanford, 1996). Mixing appears to concentrate within the  
MAW, where the shear values are the highest is strongest in the study area, and not deeper than >  
110 m, where there is no remarkable significant shear and the system is weakly stratified. The shear  
to strain ratio calculated applying the Gregg89 model ( $S_{10}^4/S_{GM}^4 = 21$ ), indicates that the energy  
435 in the IW field is higher than that of the GM model, which is usually has a value of  $\approx 3$ . We can  
therefore make the assumption that the energy is distributed in the whole inertial range where the  
water structures are stable (e.g. Munk, 1981). Similar results were obtained by Holbrook et al.  
(2013), who registered a shear to strain ratio of 17. The IWs can therefore be considered as an  
energy distributor from anisotropic to isotropic motions. The  $k_p$  value obtained from XCTD and  
440 ADCP using Gregg89 model is  $k_p \approx k_0 \approx 10^{-3.0} m^2 s^{-1}$ , whereas we obtain  $k_p \approx k_0 \approx 10^{-2.7} m^2 s^{-1}$  using  
MCS data and the Batchelor59 model. The range of variation in the two cases are also comparable,  
being the maximum values of  $10^{-2.2} m^2 s^{-1}$  and  $10^{-1.5} m^2 s^{-1}$ , and the minimum values of  $10^{-5.4} m^2 s^{-1}$  and  
 $10^{-5.7} m^2 s^{-1}$ , respectively, for the two methods. These similar values obtained based on different  
models and using independent techniques are well above the global average, suggesting that the  
445 downward energy transfer cascade to small scales is highly efficient in the studied surveyed area.

We find no direct clear correlation between local  $k_p$  variations and the presence of IWs and  $k_p$ .  
Thus, we interpret individual IWs, which are clearly imaged and display a rather homogeneous  
distribution all along the line. Conversely, we find some hints of a direct relationship between  
450 changes in the amplitude of vertical isopycnal displacements and variations in  $k_p$  (Figs. 7 and 8),  
or between local peaks in the amplitude of vertical displacement and high  $k_p$ , in the transitional  
domain. Our interpretation is that IW-induced mixing is probably not efficient enough to keep the  
overturning in the target area (Figs. 7 and 8). No clear. Instead, the correspondence between IW  
amplitude and  $k_p$  variation is found along any of the three reflectors. This high-amplitude features

Formatted: Font: Times New Roman, 12 pt

Formatted: Font: Times New Roman

Formatted: Font: Italic, Subscript

Formatted: Font: Times New Roman

455 in the shear instability-dominated transitional domain with  $k_p$ , suggests that the energy transfer  
between IWs and turbulence is probably enhanced by shear instabilities. The lack of clear  
correlation between IWs and turbulence agrees with Klymak and Moum (2007) Moum's (2007a)  
assumption, suggesting a weak dependence of mixing rates on IW energy. The mixing rates are  
460 more reliably measured at Our observations indicate that the processes of IW destabilization and  
breaking appear to be important to allow transferring energy towards smaller scale regimes, in  
this scales efficiently and enhance mixing. In the case the instability dominated regime that  
encloses the transition towards turbulence. In our case, a number of of the Alboran thermocline, the  
main mechanism could well be the development of shear instabilities, but other processes such as  
465 the interaction of IWs with rough bathymetry could also play an equivalent role in other regions  
and settings (Dickinson et al., 2017).

The "mixing patches" have been hotspots identified at specific locations in the  $k_{pD}(x,z)$  map (Fig.  
3), which appear to spatially coincide with areas where shear instability features are located (see  
reflectors H1 and H3 in figs. 7, 9). These mixing hotspots likely represent a significant source of  
470 regional diapycnal mixing at the boundary layer between the MAW and the MW (30 – 200 m),  
which is subject to vertical stratification and shear values of  $3.2 \times 10^{-3} s^{-1}$ . The mixing and energy  
transfer between these two water masses constitutes the main energy source of the region. The  
In contrast to other regions (i.e. the Gulf of Mexico as in Dickinson et al., 2017), the smooth and  
475 relatively deep seafloor along the profile (> 800 m in average; fig. 10b), likely Fig. S4c) suggests  
a small contribution to of interaction with bathymetry in the generation of the mixing hotspots.  
Given that the MAW-MW boundary layer is subject to shear (Fig. 10a S4a, and S4b), and taking  
into account the visual correspondence between the location of the largest amplitude features in  
the instability dominated transitional domain and high mixing values along individual reflectors,  
480 we hypothesize that the existence of a direct cause of link between mixing hotspots is the  
development of and IW shear instabilities. This could explain both the peak values of  $k_p$  and the  
high mixing variability along the profile throughout the surveyed area despite the ubiquitous  
presence of IWs.

The  $k_p k_D$  values along H1 are over the global average for overturning along most of the reflector  
485 ( $\langle k_p k_D \rangle \approx 10^{-2.5} m^2 s^{-1}$ ), with lower values only at some specific points locations (Fig. 7a). These  
points are located to the right of 34.7 km, where  $k_p$  sharply decreases. A similar situation is also  
observed along H3, reaching a global average ( $\langle k_p k_D \rangle \approx 10^{-3.4} m^2 s^{-1}$ , 7b). The spatial correspondence  
between high diffusivity values and the presence of large-amplitude features at the transitional  
490 subrange, interpreted to correspond to KH-like shear instabilities by (Sallares et al., 2016) at the  
transitional subrange, is consistent with the hypothesis that a causal relationship exists between  
the two. This is conceptually equivalent to the mechanism proposed by Gregg (1987), where  
mixing at the transitional subrange occurs principally at vortex sheets through wave-instability.  
We could therefore As an example, we hypothesize that in horizon H1, the presence of a vortex  
sheet left of 34.7~35 km along profile produces the high mixing values, whereas to the right, there  
495 is no vortex sheet and the ocean is more stable. Similar results suggesting The correspondence  
between diapycnal peaks and wave-instabilities in horizon H3 suggests a similar situation (Fig. 8).  
Our results indicating a patchy ocean interior, although at larger scales and deeper levels, were  
also coincide with those previously presented by Sheen et al. (2009) and Fortin et al. (2016). Our  
500 ), and Dickinson et al. (2017), but our work confirms these previous results and suggests that  
allows extending the variation is probably due conclusions to smaller scale-processes and shallower

Formatted: Font: Italic

ocean levels. Additionally, we identify the high mixing induced by the development of shear instabilities, which enhances in turn as a likely relevant mechanism driving the downward energy transfer to small scales, cascade between IWs and turbulence at the thermocline depth that should be taken into consideration in ocean dynamic models.

505

## 5. CONCLUSIONS

We have used acoustic images obtained with a high-resolution MCS system to produce a 2D diapycnal mixing map around the thermocline depth of the Alboran Sea. Our results confirm a high level of diapycnal variability and the presence of marked mixing patches/hotspots in the water column. The  $k_p(x, z)$  map obtained by applying the Batchelor59 model to the seismic data, has a strong variability with values ranging between  $\langle k_p \rangle \approx k_D \approx 10^{-1.5} m^2 s^{-1}$ , in the high mixing patches (brightest hotspots), and  $\langle k_p \rangle \approx k_D \approx 10^{-3.3} m^2 s^{-1}$ , for in the background values. The obtained values are high enough to account for overturning at thermocline depths. The mixing hotspots have a characteristic size of 10-15 m in the vertical dimension, and 1-2 km in the horizontal one, although there are also some smaller-size ones. They are located at different depths within the thermohaline layer, although they appear to concentrate in highly sheared regions. The comparable values obtained with the two independent methods XCTD- and approaches ADCP-based measures, confirm that HR-MCS is a useful technique to study processes and structures occurring at the sub-mesoscale, which are difficult to be studied otherwise capture and characterize by other means.

510

515

520

Formatted: Font color: Custom Color(RGB(0,0,10))

Formatted: Font: Times New Roman, Font color: Custom Color(RGB(0,0,10))

We investigate the relationship between mixing variability and ocean dynamics at different spatial scales is investigated by analyzing the spectral amplitudes along two/four seismic horizons in the internal waves and transitional, or instability-dominated, subranges. On one hand, we found no clear correspondence between the location of the mixing patches and the location and amplitude of individual IWs, which are imaged all along the surveyed area. Conversely, a visual correspondence exists between the location of shear instabilities/high-amplitude isopycnal vertical displacements at the instability-dominated transitional subrange and high mixing hotspots values in different reflectors, suggesting a causal relationship between both features. We interpret the development of shear instabilities as a mechanism that locally enhance downscale energy transfer between IWs and turbulence. Areas displaying the most vigorous instabilities coincide with the highest estimated diapycnal mixing values, which are well above the global average global value for meridional overturning. This observation suggests that the energy transfer from anisotropic to isotropic scales is highly efficient at thermocline depths within the studied area.

525

530

535

Formatted: Font: Times New Roman

Formatted: Normal

Formatted: Font: Times New Roman

Formatted: Font: Times New Roman

Formatted: Font: Times New Roman

Formatted: Font: Times New Roman

Formatted: Font: Times New Roman

Formatted: Font: Times New Roman

Formatted: Font: Times New Roman

Formatted: Font: Times New Roman

Formatted: Font: Times New Roman

Formatted: Font: Times New Roman

Formatted: Font: Times New Roman

Overall, our study shows that the HR-MCS technique can be used to study sub-mesoscale structures and processes at the thermocline level, provided that the stratification is strong enough to produce acoustic reflectivity that can be recorded by the system. The high-resolution 2D maps produced from the seismic reflectivity could help improving the estimates of the parameters to be incorporated in numerical models of ocean dynamics.

540

## ACKNOWLEDGEMENTS

Formatted: Font: Times New Roman

This work has been fulfilled in the framework of the projects POSEIDON (Ref: CTM2010-25169) and APOGEO (Ref: CTM2011-16001-E/MAR), both funded by the Spanish Ministry of Economy

545 and competitiveness (MINECO). The seismic and oceanographic data were acquired in the  
 framework of the IMPULS survey (Ref: 2003-05996-MAR) also from MINECO, and SAGAS  
 survey (Ref: CTM2005-08071-C03-02/MAR-SAGAS). Helpful comments were provided by  
 Josep Lluís Pelegrí, Miguel Bruno, numerous colleagues at the Barcelona Center for Subsurface  
 Images (B-CSDI), and Diana Francis and David M. Holland from the Center for Global Sea Level  
 550 Change (CSLC) – NYUAD, Abu Dhabi, UAE.

## APPENDIX A

Table A1. Parameters used in text

Variable	Value	Description
$f$	$0.00008613 \text{ s}^{-1}$	Coriolis f. at $36^\circ$
$N$	$5 \text{ cph} = 0.00138 \text{ s}^{-1}$	Buoyancy frequency (ocean average)
$V$	$0.207 \text{ m s}^{-1}$	RMS amplitude of velocity fluctuations
$\nu$	$0.000001064 \text{ m}^2 \text{ s}^{-1}$	Kinematic Viscosity
$C_T$	0.4	Proportionality constant
$\Gamma$	0.2	Empirical value of mixing efficiency (Osborn and Cox, 1972).

555

## APPENDIX B

Buoyancy Reynolds number

560

Gargett et al, (1988) use an index to know if the system is isotropic or not, and hence if the allowing  
 know to determine if the buoyancy flux is substantial/vigorous enough to generate turbulence and  
 therefore a high mixing level (Thorpe, 2005). The index depends on kinematic viscosity and is  
 called Buoyancy Reynolds number:

565

$$R_B = \varepsilon / \nu N^2$$

(B1)

570

The mean kinematic viscosity in the ocean is  $\nu = 1 \times 10^{-6} \text{ m}^2 \text{ s}^{-1}$ . Some properties of the inertial  
 subrange are consistent with isotropy for values of  $R_B < O(10^2)$ . To consider anisotropy and avoid  
 serious underestimates of mixing, Smyth and Moum (2000) propose that values  $> 200$  are related  
 with confidence to a safe value for high mixing levels due to free viscous effects. For our  
 submesoscale regime  $R_B = 3200$ , a value that reasserts is compatible with the coherence of  
 the calculated mixing levels. The MCS data present a high confidence level.

575

## References

Formatted: Font: Times New Roman, 12 pt

Formatted: Font: Times New Roman, 12 pt

- Biescas B., B. R. Ruddick, M. R. Nedimovic, V. Sallarès, G Bornstein, and J. F. Mojica, Recovery of temperature, salinity, and potential density from ocean reflectivity, *J. Geophys. Res. Oceans*, 119, 3171-3184, doi:10.1002/2013JC009662, 2014.
- 580 Batchelor G. K., Small-scale variation of convected quantities like temperature in turbulent fluid, *Fluid Mech.*, 5, 113-133, 1959.
- Chioua J., Bruno M., Vazquez A., Reyes M., Gomiz J., Mañanes R., Alvarez O., Gonzalez C., Lopez L., Gomez-Enri J., Internal waves in the strait of Gibraltar and their role in the vertical mixing processes within the bay of Algeciras, *Estuarine, Coastal and Shelf Science*, Elsevier, 126, 70-86, 2013.
- 585 D'Asaro Eric A., Lien Ren-Chien, The Wave-turbulence transition for stratified flows, *Journal of physical Oceanography*, 1669-1678, July, 2000.
- 590 Dickinson, A., White, N. J., Caulfield, C. P., Spatial variation of diapycnal diffusivity estimated from seismic imaging of internal wave field, Gulf of Mexico. *Journal of Geophysical Research: Oceans*, 122, 9827-9854. <https://doi.org/10.1002/2017JC013352>, 2017.
- Ferrari Raffaele and Wunsch Carl, Ocean circulation kinetic energy: Reservoirs, sources, and sinks, *Annu. Rev. Fluid Mech.*, 41: 253-282, 2009.
- Fortin W., et. al., Mapping turbulent diffusivity associated with oceanic internal lee waves offshore Costa Rica. *Ocean Sci.*, 12, 601-612, 2016.
- 595 Gargett A and Holloway G, Dissipation and diffusion by internal wave breaking, *J. Mar. Res.*, 42, 15-27, 1984.
- Gargett A., The scaling of turbulence in the presence of stable stratification, *J. of Geophys. Res.*, 93, 5021-5036, 1988.
- 600 Garrett Christopher and Munk Walter, Internal waves in the ocean, *Ann. Rev. Fluid Mech.*, 11, 339-369, 1979.
- Gibson Carl., Keeler R., Bondur Valery, Leung Pak, Prandke H., Vithanage D., Submerged turbulence detection with optical satellites, *Coastal Ocean Remote Sensing Conf.*, Paper 6680-33, San Diego, CA, 2007.
- 605 Gregg M. C., Diapycnal mixing in the thermocline: A review, *Journal of geophysical research*, Vol. 92, Number C5, 5249-5286, 1987.
- Gregg M. C., Scaling turbulent dissipation in the thermocline, *Journal of geophysical research*, Vol. 94, Number C7, 9686-9698, 1989.
- Haibin Song, Luis M. Pinheiro, Barry Ruddick and Xinghui Huang. *Seismic Oceanography: A new geophysical tool to investigate the thermohaline structure of the oceans*, Oceanography, Prof. Marco Marcelli (Ed.), ISBN: 978-953-51-0301-1, InTech, 2012.
- 610 Henyey Frank S. and Wright Jon, Energy and action flow through the internal wave field: an Eikonal Approach, *Journal of Geophysical Research*, Vol. 91, No: C7, Pages 8487-8495, July 15, 1986.
- 615 Holbrook, W., Fer, I., Ocean internal wave spectra inferred from seismic reflection transects. *Geophysical Research Letters*, Vol. 32, L15604, doi:10.1029/2005GL023733. 2005.
- Holbrook, W., Fer, I., Schmitt, R., Lizarralde, D., Klymak, J., Helfrich, C. and Kubichek, R., Estimating oceanic turbulence dissipation from seismic images, *Journal of Atmospheric and Oceanic Technology*, 2013. *Annu. Rev. Fluid Mech.*, 40, 169-184, 2008.
- 620 Holbrook Steven, Fer Ilker, Schmitt Raymond, Lizarralde Daniel, Klymak Jody, Helfrich Cody, and Kubichek Robert, Estimating oceanic turbulence dissipation from seismic images, *J. of Atmospheric and Oceanic Tech.*, Vol. 30, 1767-1788, doi:10.1175/JTECH-D-12-00140.1, 2013.

- Klymak M. Jody, Moun N. James, Oceanic isopycnal slope spectra. Part a: Internal waves, *Journal of Physical Oceanography*. American Meteorological Society, Vol. 37, 1215-1231, 2007.
- 625 Klymak M. Jody, Moun N. James, Oceanic isopycnal slope spectra. Part b: Turbulence, *Journal of Physical Oceanography*. American Meteorological Society, Vol. 37, 1232-1244, 2007.
- Kolmogorov, A., Dissipation of energy in the locally isotropic turbulence (English translation 1991). *Proc. Roy. Soc. London*, A434, 15–17. 1941.
- 630 Kunze, E., and Thomas B. Sanford. Abyssal Mixing: Where it is not. *J. Phys. Oceanogr.* 26, 2286-2296, 1996.
- Laurent and Garrett, The role of internal tides in mixing the deep ocean. *J. Phys. Oceanogr.* 32, 2882-2899, 2002
- Li Hua, Yamazaki Hidekatsu, Observations of Kelvin-Helmholz billow in the ocean, *Journal of Oceanography*, Vol. 57, 709-721, 2001.
- 635 Munk W. H., A survey of internal waves and small-scale processes, *Evolution of Physical Oceanography*, edited by B. A. Warren and C. Wunsch, pp. 264-291, MIT Press, Cambridge, Mass, 1981.
- Munk W. Wunsch C., Abyssal recipes II: energetics of tidal and wind mixing, *Deep-Sea Research I*, Vol. 45, 1977-2010, 1998.
- 640 Müller, P. and R. Pujale : Internal gravity waves and small scale turbulence, proceeding, ‘Aha Huliko’ a Hawaiian winter workshop, Hawaiian institute of geophysics, Special Publications, 299 pp., 1984.
- Osborn T., & C. S. Cox, Oceanic fine structure, *Geophys. Fluid Dyn.*, Vol. 3, 321-345, 1972.
- 645 Osborn T. R, Estimates of the local rate of vertical diffusion from dissipation measurements, *Journal of Physical Oceanography*, Vol. 10, 83-89, 1980.
- Riley J. James, Stratified turbulence: A possible interpretation of some geophysical turbulence measurements, *Journal of the Atmospheric Sciences*. Vol. 65, 2416-2424, 2008.
- Sallarès, V., J. F. Mojica, B. Biescas, D. Klaeschen, and E. Gracia, Characterization of the submesoscale energy cascade in the Alboran Sea thermocline from spectral analysis of high-resolution MCS data, *Geophys. Res. Lett.*, 43, 6461-6468, doi:10.1002/2016GL069782.
- 650 Samodurov, A., S., Lubitsky, A., A., and Panteleev, N., A., Contribution of breaking internal waves to structure formation, energy dissipation, and vertical diffusion in the ocean. *Phys. Oceanogr.*, Vol. 6, 3, pp 177 - -190, 1995.
- Send Uwe, Font Jordi, Krahnemann Gerd, Millot Claude, Rhein Monica, Tintore Joaquin, Recent advances in observing the physical oceanography of the western Mediterranean Sea. Elsevier Science. *Progress in Oceanography*. Vol. 44, 37-64, 1999.
- 655 Sheen L. K., White J. N., Hobbs R. W., Estimating mixing rates seismic images of oceanic structure, *Geophysical Research Letters*, Vol. 36, L00D04, 2009.
- Sheriff Robert and Geldart Lloyd, *Exploration Seismology*, Cambridge University Press, Second edition, 1995.
- 660 Smyth W. D., Moun J. N., Nash J. D., Narrowband oscillations in the upper equatorial ocean. Part II: Properties of shear instabilities, *Journal of Physical Oceanography*. American Meteorological Society, Vol. 41, 412-428, 2011.
- Sreenivasan Katepalli, The passive scalar spectrum and the Obukhov-Corrsin constant, *Phys. Fluids*, 8, 189-196, 1996.
- 665 Smyth William D., Moun James N., Anisotropy of turbulence in stably stratified mixing layers, *Physics of Fluids*, 12, No. 6, 2000.

- Smyth William D., Moum James N., Ocean mixing by Kelvin-Helmholtz Instability, Oceanography, Vol. 25, No. 2, June 2012.
- 670 Stewart Robert, Introduction to Physical Oceanography, Department of Oceanography, Texas A&M University, 2008.
- Taylor G. I., The spectrum of turbulence, Proc. R. Soc. Lond. A., Vol. 164, No. 919, 476-490, 1937.
- 675 Thorpe S. A., Experiments on the instability of stratified shear flows: miscible fluids, J. Fluid Mech., Vol. 46, 299-319, 1971.
- Thorpe S. A., The turbulent ocean, Cambridge University Press, Cambridge, 2005.
- Waite, Michael L., Stratified turbulence at the buoyancy scale, Physics of fluids, American Institute of Physics, 23, 066602-1, June 2011.
- 680 Wesson J.C. and Gregg M.C., Mixing at camarinal sill in the strait of Gibraltar, Journal of Geophysical Research, Vol. 99, No. C5, pages 9847-9878, May 15, 1994.
- Woods, J., D.,: Wave induced shear instability in the summer thermocline, J. Fluid Mech., 32, 791-800., 1968.
- Wunsch Carl and Ferrari Raffaele, Vertical Mixing, energy, and the general circulation of the oceans, Annual Review Fluid Mech. 36, p. 281-314, 2004.
- 685 Yilmaz, O., and S. M. Doherty, Seismic Data Processing, Soc. Of Explor. Geophys, Tulsa, Okla 1987

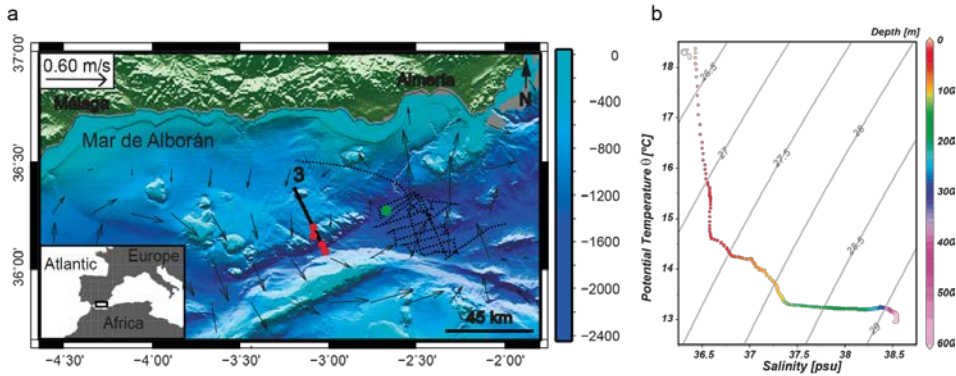


Figure 1. (a) Bathymetric map of the Alboran Sea and location of the data used in the study. HR-MCS profile acquired during the IMPULS-2006 experiment (black line labelled 3), eXpendable Bathy-Thermograph (XBTs) profilers (red circles), eXpendable Conductivity Temperature Depth (XCTD) probe (green circle). Acoustic Doppler Current Profiler (ADCP) lines (black dotted line). Geostrophic velocity for May 17<sup>th</sup>, 2006 (gray arrows). (b) Temperature-Salinity diagram from XCTD probe.  $\sigma_0$  is the potential density in  $\text{kg/m}^3$ . Color scale indicates depth.

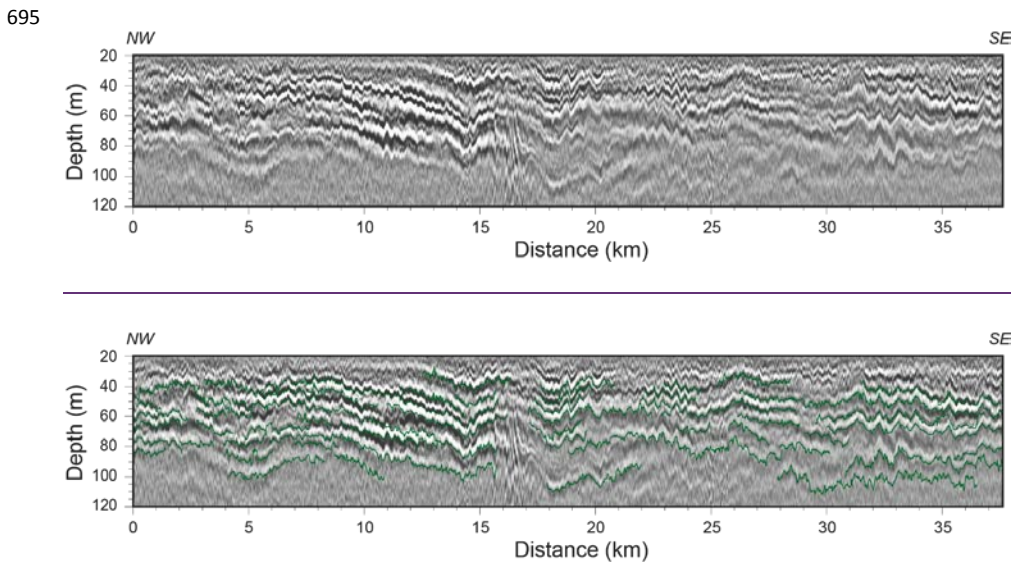


Figure 2. Depth-converted high-resolution multichannel seismic profile, with the tracked reflectors superimposed (green lines). (See Fig. 1a for location).

700



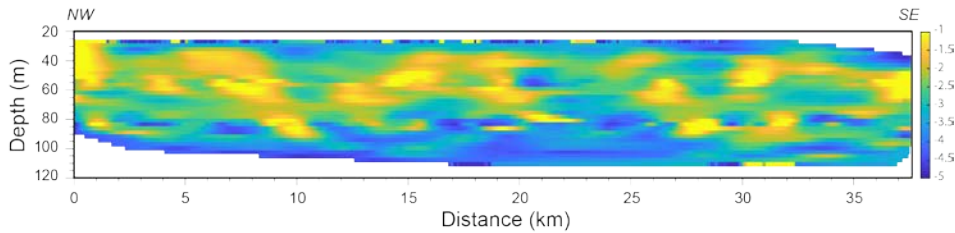
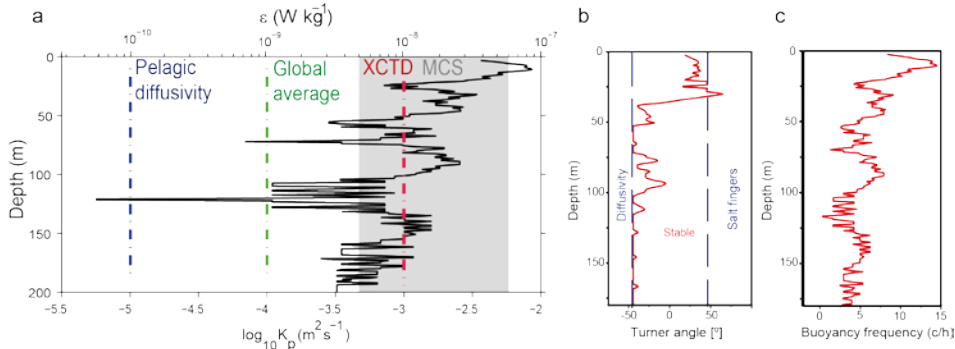


Figure 3.  $k_p(x, z)$  map obtained along the seismic profile indicated in Fig. 1, following the procedure explained in the text. White colored areas correspond to poorly sampled areas, with too few data to properly calculate  $k_p$ .

Formatted: Font: Times New Roman

705



710 Figure 4. (a) Depth profile of  $\epsilon(z)$  and  $k_p(z)$  obtained from XCTD and ADCP data and applying Gregg89 model. The blue dotted line is the pelagic diffusivity in the ocean ( $k_p \approx 10^{-5} m^2 s^{-1}$ ), the  
 715 global average for overturning ( $k_p \approx 10^{-4} m^2 s^{-1}$ ), the red dotted line is the average vertical profile from XCTD and ADCP data ( $k_p \approx k_p \approx 10^{-3.0} m^2 s^{-1}$ ) and the gray area is the incidence range from MCS data ( $k_p \approx k_p \approx 10^{-2.7} m^2 s^{-1}$ ). (b) Turner angle showing ranges, the blue dotted lines shows where the water column is unstable to diffusivity ( $Tu < -45^\circ$ ), stability ( $-45^\circ < Tu < 45^\circ$ ) and prone to salt fingering ( $Tu > 45^\circ$ ), and (c) buoyancy profile calculated with the XCTD data.

Formatted: Font: Times New Roman

Formatted: Font: Times New Roman

Formatted: Font: Times New Roman

Formatted: Font: Times New Roman, 12 pt

Formatted: Font: Times New Roman, 12 pt

Formatted: Font: Times New Roman, 12 pt

Formatted: Font: Times New Roman, 12 pt

720

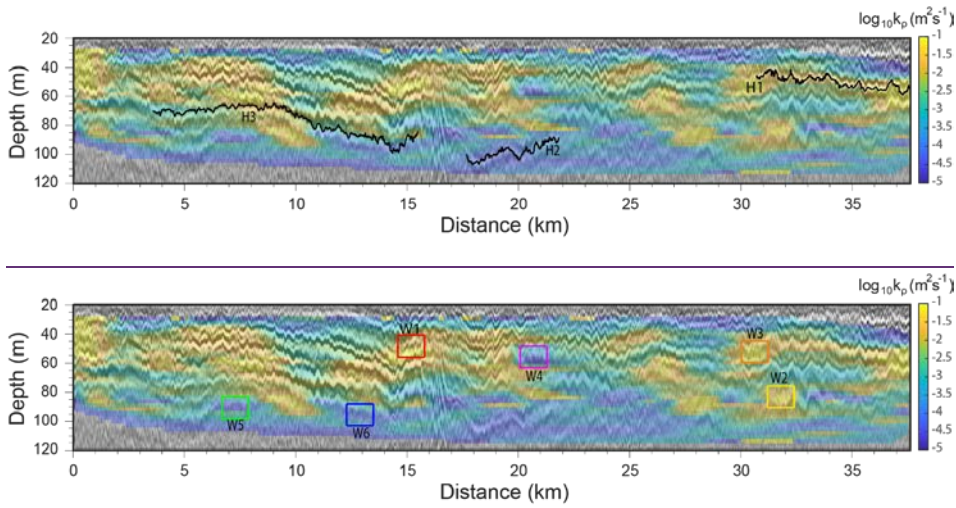


Figure 5. High-resolution  $k_p(x, z)$  map overlapped with the HR-MCS image. Solid lines labelled H1, H2 and H3, display acoustic reflectors located within relatively Squares indicate location of some of the  $1200\text{ m} \times 15\text{ m}$  windows analyzed. They have been selected as examples of high-dissipation (windows W1-W3) and low-dissipation areas from Batchelor model (windows W4-W6) areas. The color code of the squares is the same as for reflector spectra in Fig. 6, so that colors coincide with those of displacement spectra within the corresponding window.

Formatted: Font: Times New Roman

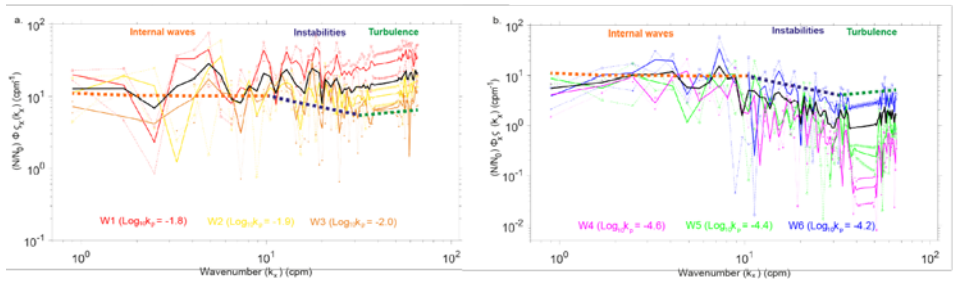
725

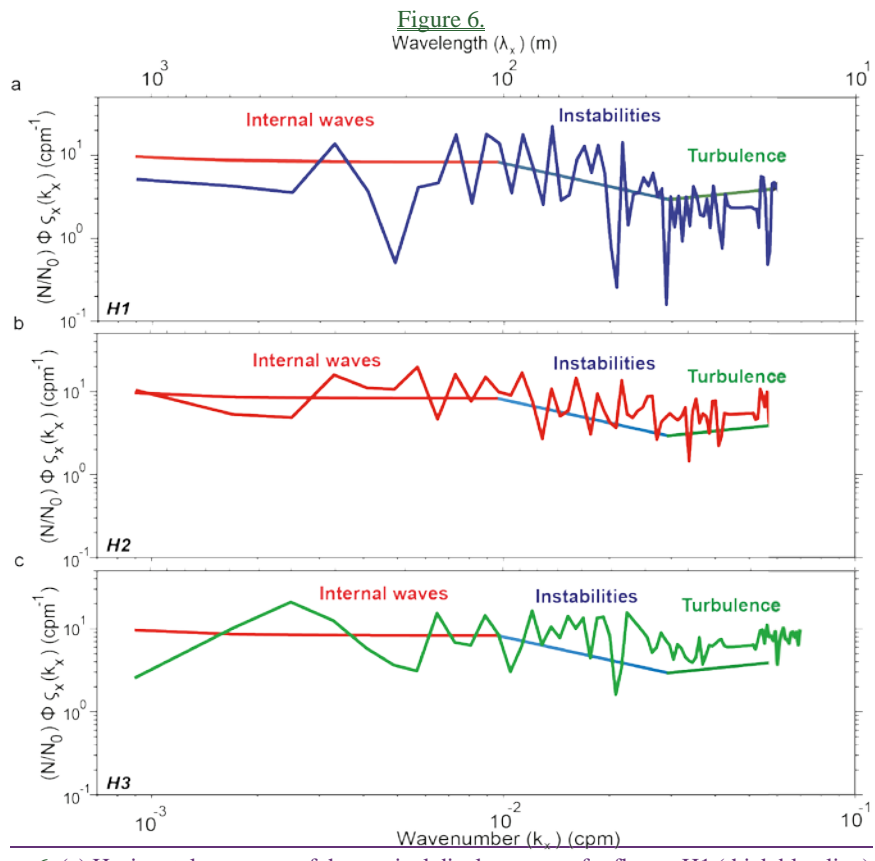
730

Formatted: Default Paragraph Font

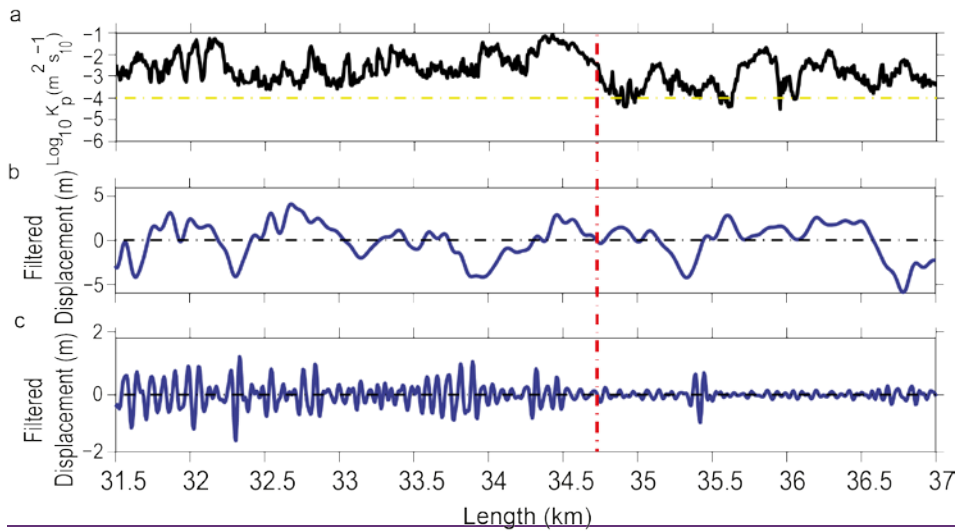
Formatted: Indent: Left: 0", First line: 0"

735





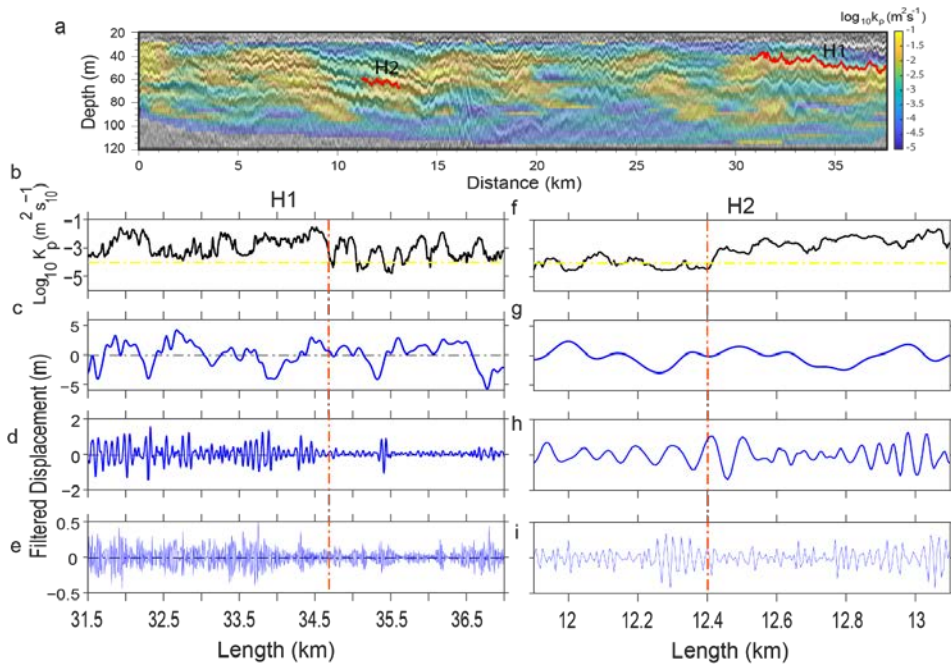
740 **Figure 6.** (a) Horizontal spectrum of the vertical displacement of reflector H1 (thick blue line) (see  
 741 location in Fig. 5). Reference line that follows theoretical slopes of Garret Munk internal wave  
 742 model (Garret and Munk, 1979) (red line), Kelvin-Helmholtz instabilities (Waite, 2011) (blue  
 743 line), and Batchelor model for turbulence (Batchelor, 1959) (green line). The methodology applied  
 744 to calculate the spectra is described in Sallares et al (2016). (b) and (c) same as in (a) for reflector  
 745 H2 (red) and H3 (green) in this case.



Average horizontal spectrum of the vertical displacements of reflectors inside windows W1-W6 (see location and color code in Fig. 5). (a) Spectra of individual reflectors in “high diffusivity” areas (thin dotted lines), average within windows W1 (red solid line), W2 (yellow solid line), and W3 (orange solid line), and average of the three “high diffusivity” windows (thick solid black line). (b) Spectrum of individual reflectors in “low diffusivity” areas (thin dotted lines), average within windows W4 (magenta solid line), W5 (green solid line), and W6 (blue solid line), and average of the three “low diffusivity” windows (thick solid black line). The reference lines are the theoretical slopes corresponding to the GM79 model for the internal wave subrange (brown dotted line), Kelvin-Helmholtz instabilities for the transitional subrange (dark blue dotted line), and Batchelor59 model for turbulence (dark green dotted line). Legend: Values of diapycnal diffusivity using spectral values at the turbulent subrange within each of the analyzed windows (same color code as for windows W1-W6).

750

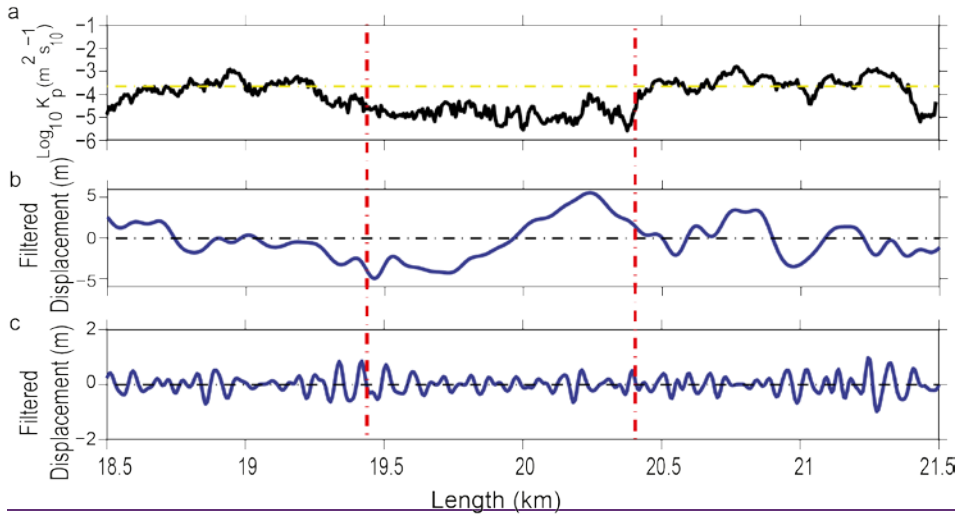
755



760

Figure 7. (a) High-resolution  $k_p(x, z)$  map overlapped with the HR-MCS image. Red lines indicate location of 2 horizons analyzed (H1 and H2). They have been selected as examples of reflectors crossing higher mixing areas. (b) Diapycnal mixing obtained along H1 (see details of calculation in the text). (c) Signal filtered at wavelength ranges of the IW sub-range (3000-100 m), (d) the transitional sub-range (100-30 m), and (e) the turbulent sub-range (30-13 m). The dashed red line identifies the “breaking point” referred to in the text. (f, g, h, i) same as (b, c, d, e) for H2.

765



770

775

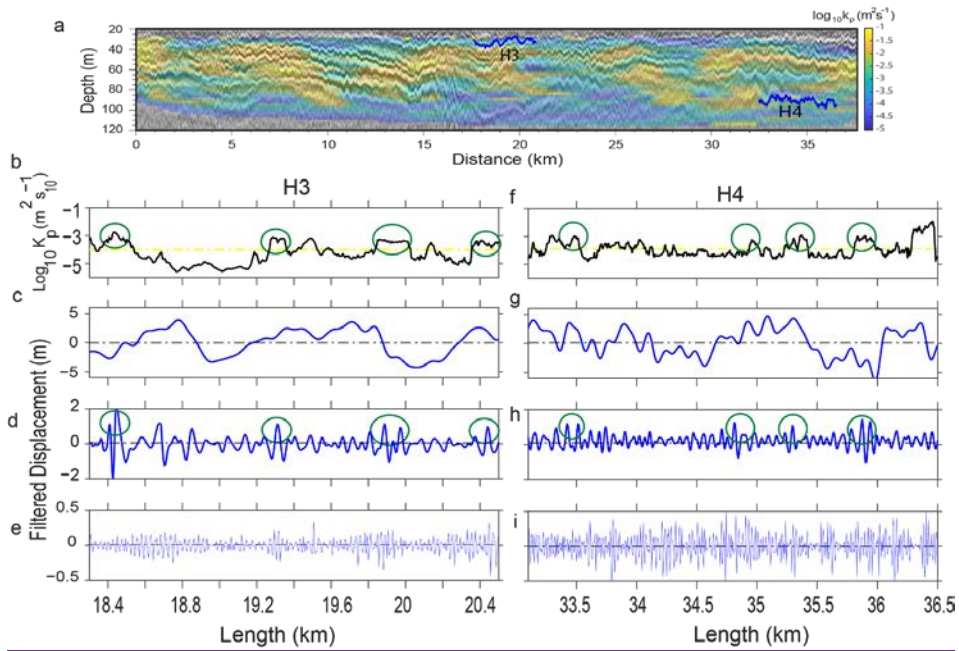
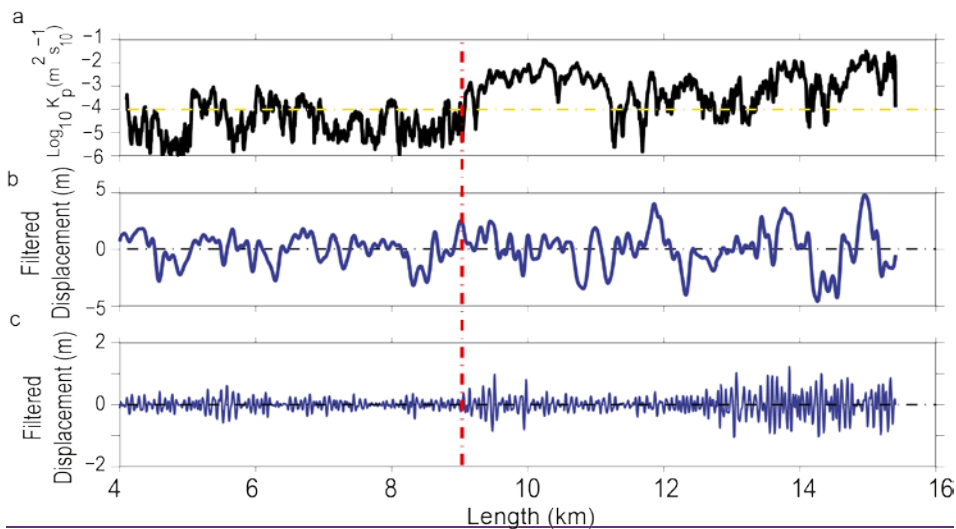


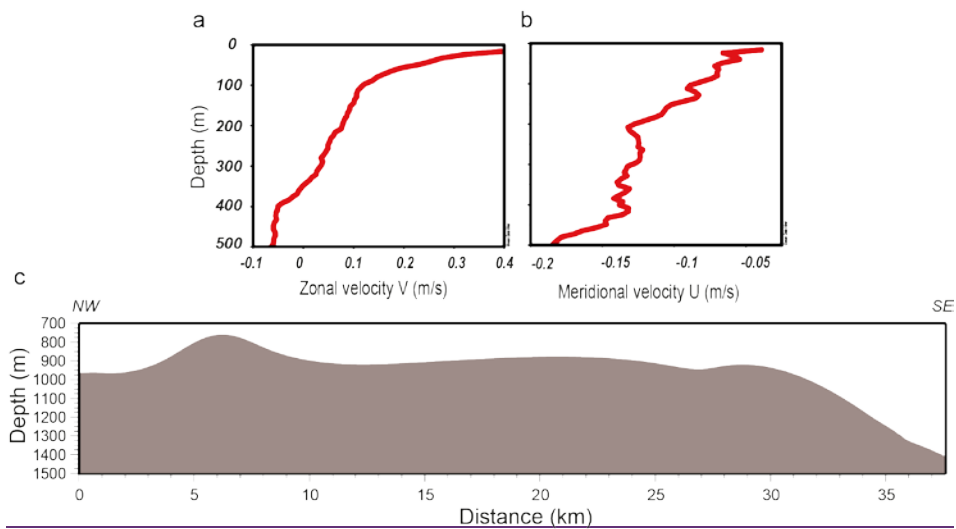
Figure 8. (a) High-resolution  $k_p(x, z)$  map overlapped with the HR-MCS image. Blue lines indicate location of 2 horizons analyzed (H3 and H4). They have been selected as examples of reflectors crossing lower mixing areas. (b) Diapycnal mixing obtained along H3 (see details of calculation in the text). (c) Signal filtered at wavelength ranges of the IW sub-range (3000–100 m), (e) and the transitional sub-range (100–33 m). The dashed red lines identifies the “breaking segment” referred to in the text.

780

785



790 **Figure 9.** (a) Diapycnal mixing obtained along H3 (see details of calculation in the text). (b)(c) Signal filtered at wavelength ranges of the IW sub-range (3000-100 m), (e) and (d) the transitional subrange (100-30 m), and (e) the turbulent subrange (30-13 m). The dashed red line identifies green circles identifies the “breaking segment diffusion peaks” referred to in the text. (f, g, h, i) same as (b, c, d, e) for H4.



795 **Figure 10**



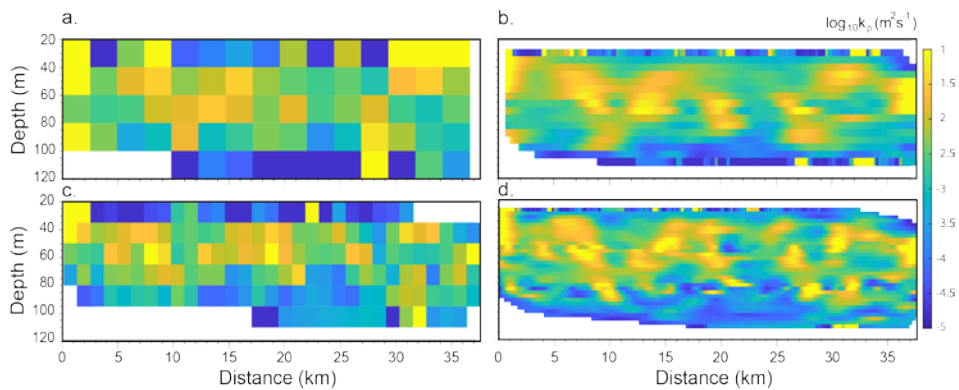


Figure S1. Four examples of  $k_\rho(x, z)$  maps obtained along the seismic profile shown in Fig.1, using windows of different size, with and without applying the sliding window approach. (a) Window size is 2400 m wide x 20 m high. (b) Same window size as in (a), but applying sliding window step of 60 m in the horizontal and 6 m in the vertical one, between neighboring windows. (c) Window size is 1200 m wide x 15 m high. (d) Same window size as in (c), but applying a sliding window step of 30 m (horizontal) and 3 m (vertical). This is the one selected and used for the analysis.

800

805

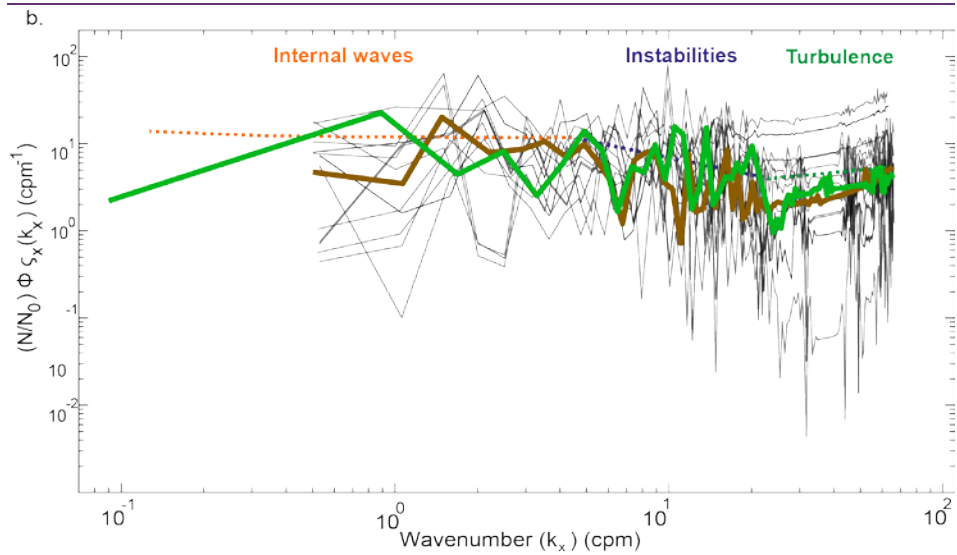
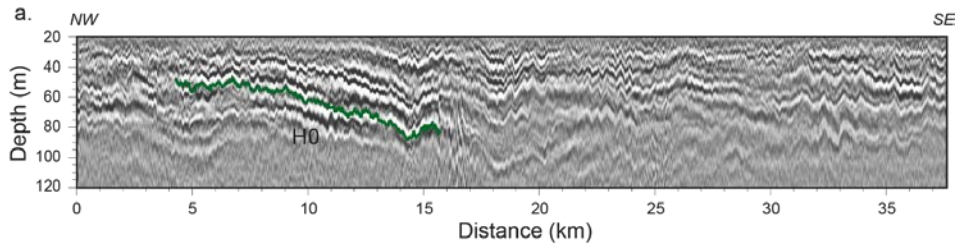
810

815

820

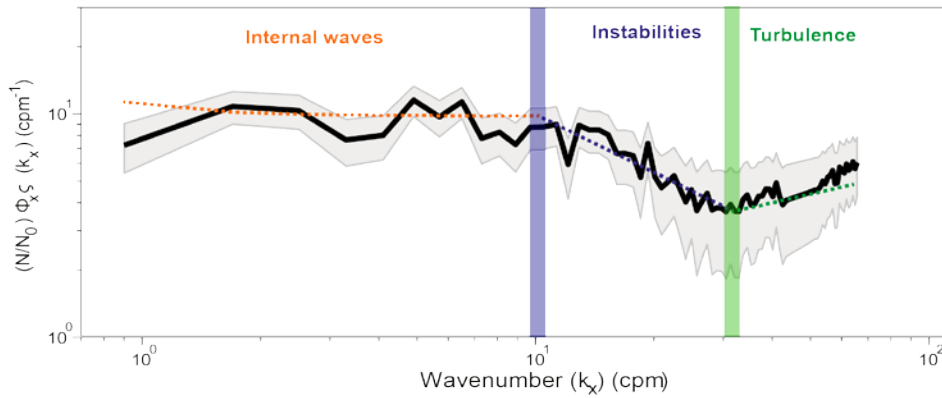
825

830

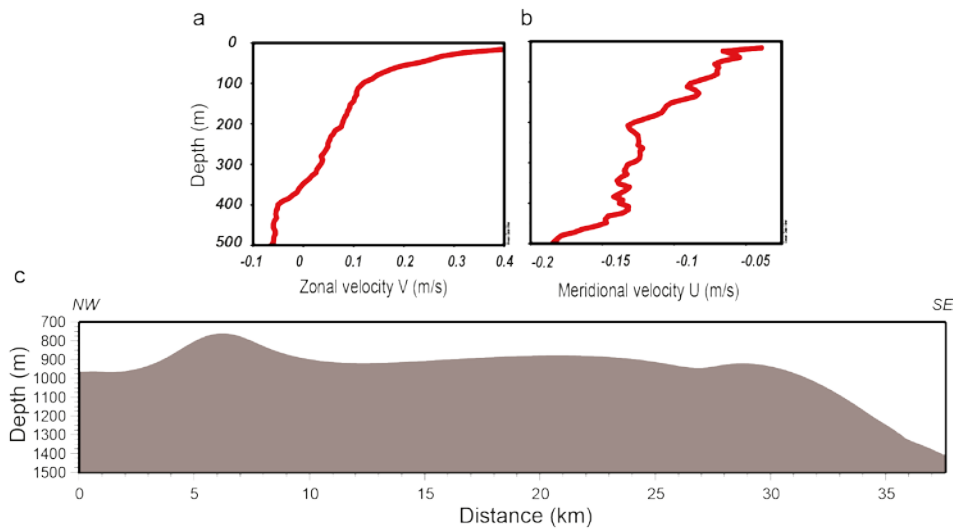


835 Figure S2 (a) Depth-converted high-resolution multichannel seismic profile (Here we show a new horizon H0, green line). (b) Horizontal spectrum of the vertical displacement of reflector H0, (green line) considering the whole reflector. (black lines) spectrum from the reflector split in ten 1.2 km-long segments. (brown line) average spectrum from the 10 segments. Segments, the average and the whole reflector show the same trends in the scales of interest.

840



845 Figure S3. Average horizontal spectrum of the 68 tracked reflectors scaled by the local buoyancy  
frequency at the reflector depth, and multiplied by  $(2\pi k_{\chi})^2$  (solid line) and its corresponding 95%  
confidence interval ( $2\sigma$ ) (shaded area). The reference lines are the theoretical slopes corresponding  
to the GM79 model for the internal wave subrange (red line), Kelvin-Helmholtz instabilities for  
the transitional/buoyancy subrange (blue line), and Batchelor59 model for turbulence (green line).  
850 The steeper slope at the highest wavenumbers corresponds to noise. The blue rectangle marks the  
buoyancy scale ( $l_N \approx 100$  m), and the green rectangle the limit between transitional and turbulent  
subranges ( $\sim 30$  m)



855 Figure S4. (a) Current velocity profile from ADCP data, SAGAS in May, 2010. (V) The zonal  
velocity variations, and (b) (U) the meridional velocity variations according to the depth. (c)  
Bathymetric profile over the seismic profile.

Formatted: Font: 12 pt

|  
860

